University of Alberta

Corrosion Behavior of Designed Ferritic-martensitic Steels in Supercritical Water

by

Zhe Liu

A thesis submitted to the Faculty of Graduate Studies and Research
in partial fulfillment of the requirements for the degree of

Master of Science
in
Chemical Engineering

Department of Chemical and Material Engineering

Spring 2013
Edmonton, Alberta

Abstract

As the Supercritical Water-cooled Reactor (SCWR) shows a promising future, the corrosion behavior of candidate materials has attracted great interest. In this study, experimental investigation was conducted to evaluate the corrosion behavior of the ferritic-martensitic steels designed for the use in SCWR. The steels were evaluated in supercritical water (SCW) with different dissolved oxygen concentrations at 500℃ and 25MPa for up to 1000 hours. The effects of alloy elements, temperature, and dissolved oxygen concentration on the corrosion behavior of the ferritic-martensitic steels in SCW have been investigated. It was found that adding Si in alloy increased the corrosion resistance, whereas the addition of Mn showed the converse effect. Higher dissolved oxygen concentration accelerated the corrosion in SCW and decreased the effects of Si and Mn. Ultrasonic peening was also investigated to evaluate its effect on the corrosion in SCW. Significant improved corrosion resistance could be achieved by ultrasonic peening treatment.

Acknowledgement

I would like to express my sincere gratitude to my research advisors, Professor Jingli Luo, and Professor Weixing Chen for providing me such a valuable research opportunity in my life, and for their countless guidance, understanding and encouragement during the course of my research.

I also would like to extend many thanks to Dr. Ming Li and Dr. Ziqiang Dong for their unselfish assistance and continuous support in helping me conduct this research. This work could not have been completed without their extensive help, for which I am really grateful.

I am also grateful for my close colleagues, Yashar Behnamian, Renfei Wang, Hao Li, Guihua Zhou and Mengshan Yu for their valuable assistance and cooperation, and also all the group members for creating such a pleasant working environment.

The funding provided by Natural Resource of Canada (NRCan), Atomic Energy of Canada Limited (AECL) and Natural Science and Engineering Research Council of Canada (NSERC) is greatly appreciated.

Lastly, I would like to dedicate this work to my beloved parents who have always unconditionally supported and guided me in my life.

TABLE OF CONTENTS

CHAPTER 1

CHAPTER 2

CHAPTER 3

CHAPTER 4

List of Tables

List of Figures

Nomenclature

H	height of sample
L	length of sample
ΔM	the weight change in in mg
M_0	weight of sample before supercritical water exposure
M_1	weight of sample after supercritical water exposure
k_p	parabolic rate constant
S	the area where oxidation took place in cm^2
t	the oxidation time
W	width of sample

Abbreviations

BWR	Boiling Water Reactor
CRIUP	Corrosion Resistance Improvement by Ultrasonic Peening
EDS	Energy Dispersive Spectrometer
LWR	Light Water Reactor
PWR	Pressurized Water Reactor
PRC	Parabolic Rate Constant
SCW	Supercritical Water
SCWR	Supercritical Water Reactor
SEM	Scanning Electron Microscopy
SS	Stainless Steel
XRD	X-Ray Diffraction

Chapter 1

Introduction

1.1 Motivation

Selecting proper candidate materials is one key issue for the development of the supercritical water-cooled nuclear reactor (SCWR). Designing or choosing the most fitting materials means better sustainability, economics and safety. As the supercritical water (SCW) is a very aggressive corrosive media, corrosion becomes one challenging problem for the materials used in the SCWR.

The corrosion performance of candidate materials in SCW can be affected by several factors, including material composition and structure, temperature and pressure of SCW, water chemistry, and exposure time. Enormous investigations have been taken to study the corrosion behavior of various candidate materials in different SCW environment, aiming to find the most fitting materials as well as an effective method to control corrosion in SCW.

Ferritic-martensitic steels have been chosen as candidate materials to be used in the SCWR. Many efforts have been made to evaluate the corrosion performance of ferritic-martensitic steels in SCW environments. Some investigations have been conducted to study the effect of chemical composition on the corrosion behavior of ferritic-martensitic (F-M) steels in SCW. However, most of those investigations only focused on the effect of chromium content. Few studies have been taken to study the effect of other alloy elements, such as Si and Mn, on the corrosion behavior of F-M steels.

Several investigations to study the effect of grain refinement on corrosion behavior of F-M steels have been conducted over the past few years. The results of these research indicated that grain refinement is an effective approach to improve the corrosion resistance of ferritic-martensitic steels in supercritical water [1, 2]. Ultrasonic shot peening has been proved to be a highly effective method for surface grain refinement [5-7]. However, little data about the effect of ultrasonic peening on corrosion behavior of F-M steels in supercritical water can be found so far.

1.2 Objectives and Scope

As a part of the Generation IV Energy Technologies program, this investigation mainly focuses on the evaluation of the corrosion behavior of ferritic-martensitic steels in SCWR environments. The corrosion control method, ultrasonic peening, was also studied. The following are the main objectives of the present study:

- Investigate the corrosion behavior of Si, Mn-containing ferritic-martensitic steels in supercritical water.

- Evaluate the effect of Si and Mn elements on corrosion behavior of F-M steels in supercritical water.
- Evaluate the influence of ultrasonic peening on corrosion behavior of ferritic-martensitic steels in supercritical water.
- Evaluate the effects of other factors, such as exposure time and dissolved oxygen concentration on the corrosion in supercritical water.

1.3 Thesis Organization

The thesis consists of 6 chapters, including introduction, and 1 appendix.

Chapter 2 is the literature review presented as background information on supercritical water, supercritical water reactor, corrosion of ferritic-martensitic steels and austenitic steels in supercritical water, corrosion control method, and ultrasonic peening .

Chapter 3 introduces the experimental procedures and test and analysis facilities used in this study, including the specimen preparation.

Chapter 4 focuses on the corrosion behavior of designed ferritic-martensitic steels in supercritical water. Oxide structure and kinetics have been presented. The effects of minor alloy elements have been discussed in details.

The discussion of the effect of surface peening on the corrosion of ferritic-martensitic stainless steel in supercritical water environments presents in Chapter 5.

Chapter 6 discusses the effect of dissolved oxygen on the corrosion of ferritic-martensitic stainless steel in supercritical water environments.

Additional information that was deemed too detailed to include in the body of the thesis is presented in appendix.

Chapter 2

Literature Review

2.1 Supercritical Water Reactor and Supercritical Water

Supercritical Water-cooled Reactor (SCWR) is one of the most promising Generation IV nuclear reactor concepts. The SCWR has many advantages over the current water-cooled nuclear reactors, such as Light Water Reactor (LWR), Pressurized Water Reactor (PWR) and Boiling Water Reactor (BWR). Figure 2.1 illustrates one design of SCWR [111]. The SCWR offers much improved thermal efficiency of 44-50%, compared to 33-35% [3] for the current-generation LWRs. A reduction in the size of the reactor coolant pumps, piping, and associated equipment can be achieved because of the higher enthalpy coolant used. There is no boiling crisis (i.e. departure from nucleate boiling or dry out) due to the lack of a second phase in the reactor, thereby avoiding discontinuous heat transfer regimes within the core during normal operation [3]. Overall the SCWR concept offers a simplified, volume reduced, safer system with high thermal efficiency.

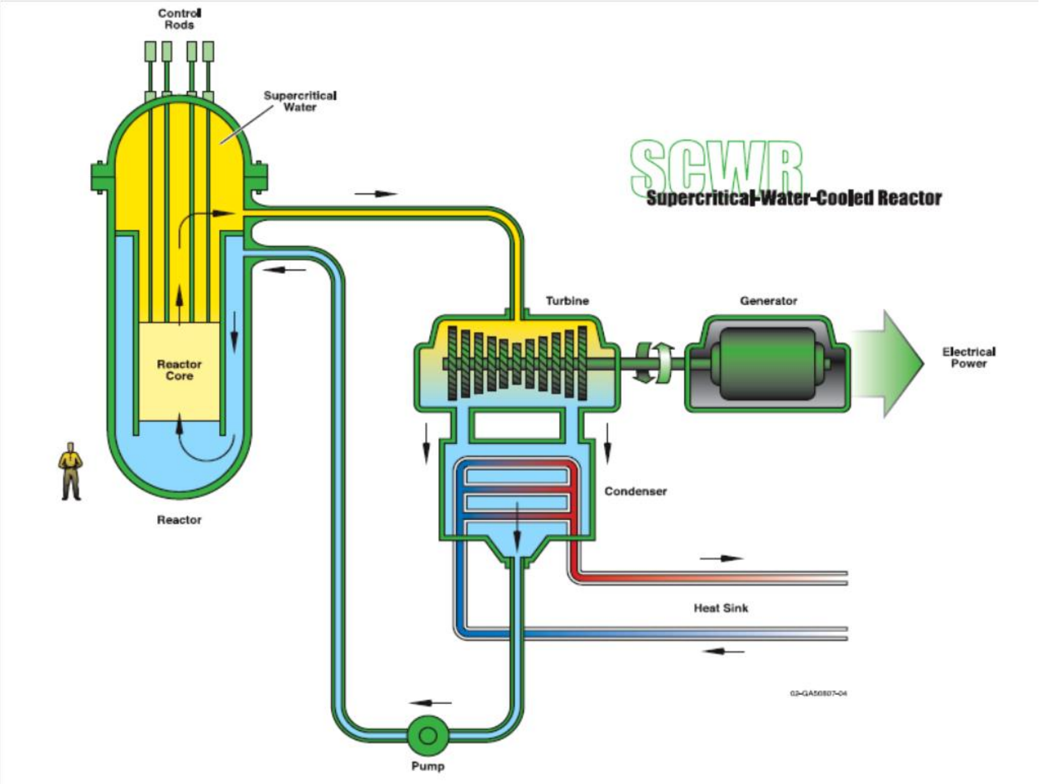

Figure 2.1 - *One SCWR system design [111].*

Supercritical water, as the water is above its critical point (374 ℃, 22.1 MPa), is a very unique chemical media. Water in supercritical state exhibits properties significantly different from those of either liquid water or vapor gas. The physical and chemical properties of supercritical water have been investigated and reviewed by E.U. Frank and co-workers in detail [25]. Supercritical water acts like a dense gas and its density can vary with temperature and pressure from less than 0.1 g/cc to values similar to that of water below the critical point. Figure 2.2 shows the density change of water when crossing the critical point [3]. At a certain temperature, a drop of density and ionic product of high-temperature water can be observed (Figure 2.3). With increasing pressure, this drop shifts toward higher temperatures and its step height decreases. Supercritical water has both liquid-like and gas-like characteristics, high diffusivity and good heat-transporting properties [3]. It is a medium with excellent transport properties, and possesses a complete solvency for most gases [5, 6] and organic compounds [7-9]. The ionic product of high-temperature water versus temperature is shown in Figure 2.4 [3]. At low pressures, water behaves as a non-polar solvent with low self-dissociation. High pressure can increase the ionic product of SCW to values above those found for water at ambient conditions. In the region near the drop of density and ionic product mentioned above, a slight change of temperature and pressure has a huge effect on the physical and chemical parameters of SCW. Chemical reactions taking place in water of high density are dominated by ionic pathways while radical reactions favor low-density water. High-density supercritical water is not only a good solvent for organic compounds, but also for gases and salts. All these special characters lead to interesting applications of supercritical water as listed in Table 2.1 [3].

Table 2.1** - Applications of supercritical water **[3].

Application	Properties exploited
Chemical reactions	High solvency for organics,
Hydrothermal syntheses	Solubility
Waste oxidation	High solvency for organics and oxygen
Radioactive waste reduction	High solvency for organics and oxygen
Biomass conversion	High solvency for organics
Plastic degradation	High solubility of monomers
Synthesis of nano-particles	Low solubility of salts

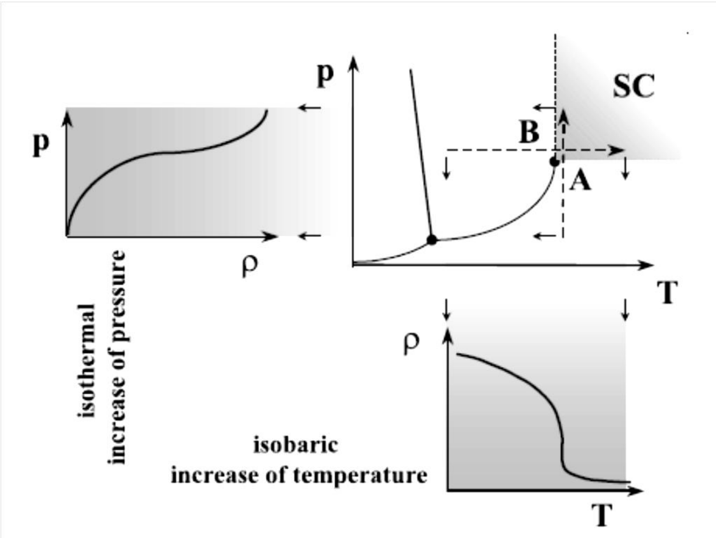

***Figure 2.2** - Phase diagram of water and schematic course of density versus pressure and temperature [3].*

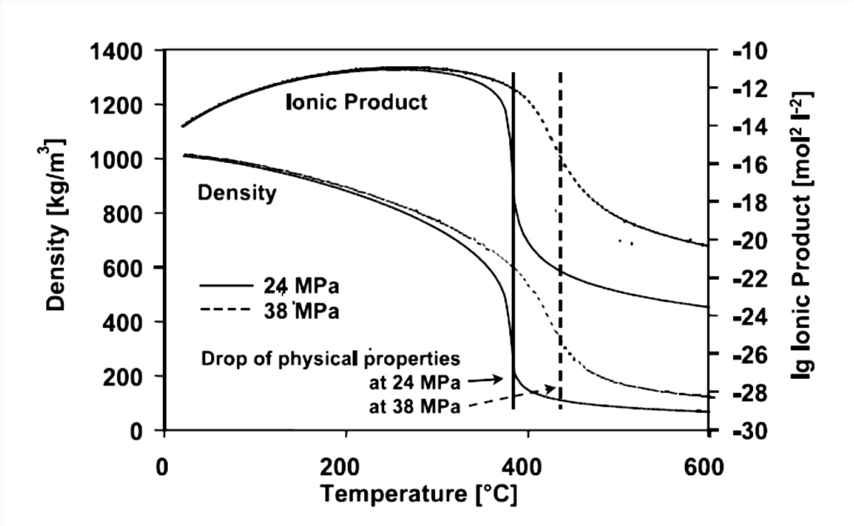

Figure 2.3 *- Drop of physical properties of high-temperature water at different pressures [3].*

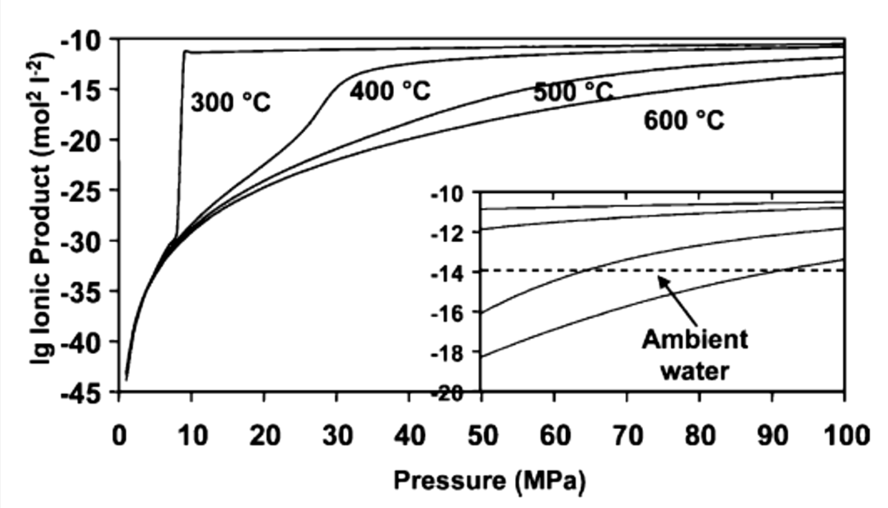

Figure 2.4 *- Ionic product of high-temperature water and steam at different temperatures versus pressure [3].*

2.2 Corrosion in supercritical water

Supercritical water at the low density is a non-polar solvent and can dissolve oxygen and other gases with complete miscibility. Depending on what species are present and how much oxygen is in the solution, supercritical water could become a very aggressive oxidizing media that may cause severe corrosion and stress corrosion cracking for the materials exposed to SCW environments.

Even with significant industry experience gained from using supercritical water in fossil plants [10, 11], there are still many challenges to use SCW in a nuclear reactor. One vital issue is caused by the geometry of the SCWR. The tubes used in a fossil-fired boiler usually have relatively thick walls, approximately 6-12 mm in thickness. In an SCWR, the wall thickness of the fuel rod cladding is 0.63 mm and the wall thickness for the water rods is 0.40 mm [3]. Therefore, the very thin components do not provide much margin for corrosion in the cores of supercritical water reactors. Oxide films of several hundred micrometer thickness are tolerant for boiler tubes with a typical wall thicknesses of 6-12 mm, but are unacceptable for water rods or fuel cladding for SCWR [13].

Another issue for developing the SCWR comes from irradiation in a nuclear reactor which can affect both the water chemistry and the alloy microstructure. Radiolysis can result in an increase in the concentration of oxygen and other oxidizing species such as H_2O_2 that raise the susceptibility to corrosion and stress corrosion cracking [3]. Radiolysis is not at all understood in supercritical water and pioneering experiments are just now underway. It is difficult to estimate the influence of irradiation on supercritical water because of the very high-temperature and significantly different properties of supercritical water compared to subcritical water. The most challenging part is the understanding of the effect of irradiation on the microstructure and how these changes influence stress corrosion cracking. Irradiation assisted stress corrosion cracking has been found on all austenitic and nickel-base alloys used in light water reactors. [16, 20]

Corrosion behavior has been studied in supercritical water for ferritic-martensitic steels, austenitic stainless steels, Ni-base alloys, Zr-base alloys, and Ti-base alloy [5-11, 99-115]. The test temperatures were generally ranged from 290 to 750 ℃ with dissolved oxygen concentration ranging from <10 ppb to 8 ppm. Exposure time for corrosion tests have ranged from 100 to over 1000 hours. In stress corrosion cracking studies, the effect of chemical species have been examined, such as H_2SO_4, HCl, H_2O_2, NaCl [3, 83, 110]. The effect of system pressure on stress corrosion cracking has been investigated as well. Kinds of test facilities, such as tube capsule, autoclave and simulative loop, made of variety of materials have been used for supercritical water exposure.

Numerous mechanisms have been proposed to for the oxidation occurred in SCW. Those models differ in the assumption of the rate-determining process: the transport mechanism through the oxide film, and the driving forces of these transport mechanisms, etc. For a particular metal, the reaction kinetics will be a function of surface characteristics of the samples, temperature, time of reaction, water chemistry and pressure.

Oxidation kinetics are commonly classified into three relationships, including logarithmic, parabolic and linear. However, those models only represent limiting and ideal cases. Deviations and intermediate rate equations are often encountered. In some cases it is difficult or even impossible to verify the validity and the correctness of the various models and parameters involved in the equations derived. Hence, it can be difficult to fit rate data to simple rate equations. In the following, a selection of the most important kinetics for high temperature oxidation will be briefly reviewed. The oxidation kinetics of a large number of metals at low temperatures (< 400 ℃) can be described by logarithmic rate equations:

Direct logarithmic:

$$x = k_{log}\log(t + t_0) + A \qquad (2\text{-}1)$$

Inverse logarithmic:

$$1/x = B - k_{il} \log t \qquad (2\text{-}2)$$

where x represents the thickness of the oxide film, t denotes the time, k_{log} and k_{il} represent the rate constants, and A and B are integration constants.

At high temperatures, the oxidation of many metals is found to follow a parabolic time dependence:

$$x^2 = k_p t + C \qquad (2\text{-}3)$$

where k_p represents the parabolic rate constant.

High temperature parabolic oxidation features that a thermal diffusion process is the rate determining process. Such a process may include a uniform diffusion of one or both of the reactants through a growing compact scale.

Linear oxidation can be described by:

$$x = k_l t + D \qquad (2\text{-}4)$$

where k_l is the linear rate constant. In contrast to the parabolic and logarithmic equations, which the reaction rates decrease with time, the rate of linear oxidation is constant with time. In this case a surface or phase boundary process or reaction may be the rate determining process [135].

2.2.1 Ferritic-martensitic steels

Ferritic-martensitic steels were selected as the candidate materials for supercritical water reactor because of their high thermal conductivity, low thermal expansion coefficients and good radiation resistance. Ferritic-martensitic steel contains two phases: ferrite and martensite. Ferrite, also known as α-ferrite (α-Fe) or alpha iron, is a materials science term for pure iron, with a body-centered cubic crystal structure. It is this crystalline structure which gives steel and cast iron their magnetic properties, and is the classic example of a ferromagnetic material [133]. Martensite is produced in carbon steels by the rapid cooling (quenching) of austenite at a high rate, in which carbon atoms do not have time to diffuse out of the crystal structure to form cementite (Fe3C). As a result, the face center cubic austinite transforms to a highly strained body centered cubic form of ferrite that is supersaturated with carbon [134].

The addition of alloy elements has great effect on microstructure and mechanical property of steels. The Si addition usually accelerates the recrystallization of ferrite during heating in the intercritical temperature range, which in turn promotes the formation of austenite through the nucleation process, followed by grain growth. Addition of Si favors the formation of a homogeneous austenite of higher hardenability resulting in a higher volume of martensite in the final structure. Thus, a silicon-bearing steel has been demonstrated to possess a higher strength in comparison with Si-free steel [139]. Manganese is added to steel to improve hot working properties and increase strength, toughness and hardenability. Manganese, like nickel, is an austenite forming element and has been used as a substitute for nickel in the A.I.S.I 200 Series of Austenitic stainless steels [138]. The addition of alloying elements also has an important impact on oxidation properties. Generally, alloying with silicon reduces the oxidation rate. The oxide scale thickness decreases with increasing Si content. This is explained by the formation of a silicon-14 rich layer at the scale/steel interface due to its less noble behaviour than iron. A SiO_2-rich inner scale layer could be observed with alloys containing Si more than 2 wt%, which results in a reduced oxidation rate [139]. The presence of the Mn element has a detrimental effect on the oxidation resistance, resulting in enhanced scale-growth rates during isothermal exposure and increased incidences of scale failure at high temperatures. This is largely due to relatively rapid diffusion of manganese across the Cr_2O_3 scale and formation of $MnCr_2O_4$ spinel on its outer surface [140].

So far, the following ferritic-martensitic steels have been studied: T91, T22, HCM12, HCM12A (T122), NF616 (T92), P2 and variety of oxide dispersion strengthened steels including JAEA 9Cr ODS, MA 956 and (14-22)Cr-4Al version [1-9]. Surface modifications, like the implantation of oxygen and yttrium and shot peening, have also been studied on ferritic-martensitic steels in SCW [3, 106, 108].

It was found that a dual-layer oxide is formed on the surface of ferritic-martensitic steel when exposed to SCW with low dissolved oxygen concentration (less than 300 ppb) [106]. A typical oxide scale with a two distinct layers was formed on ferritic-martensitic steel after SCW exposure as shown in Figure 2.5. The outer oxide layer predominantly consists of iron oxide while the inner oxide layer contains a significant amount of chromium, iron oxides. For 300 ppb and lower dissolved oxygen concentration, XRD data have indicated the outer oxide layer is magnetite and the inner layer is an iron chromium spinel $(Fe, Cr)_3O_4$ [108].

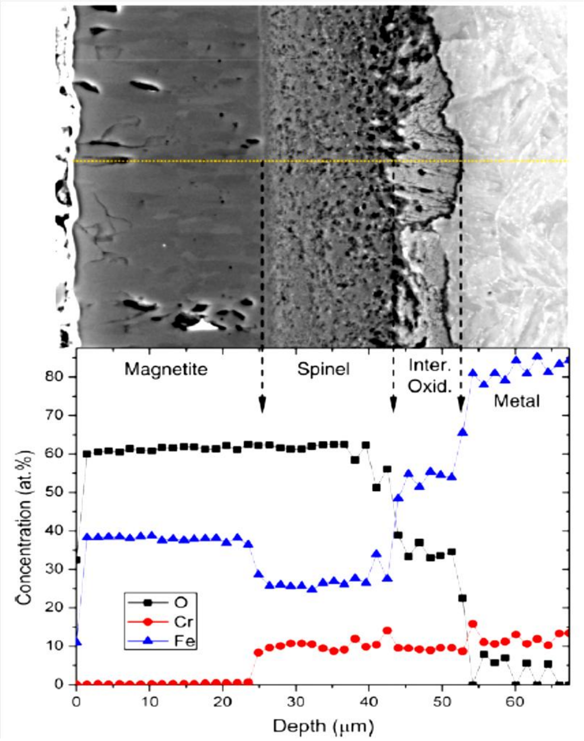

Figure 2.5 *- Cross-section image and EDS of HCM12A exposed to 600 ℃ SCW containing 25 ppb dissolved oxygen for 1026 h [3].*

For the SCW tests with high (2000 ppb) dissolved oxygen concentration, a hematite layer has been found on the dual layer oxide structure. The formation of a three-layer oxide in high oxygen concentration and a two-layer in low oxygen concentration is consistent with predicted stable phases [24]. In addition, the EDS profile in Figure 5 shows that an internal oxidation transition layer underneath the inner spinel layer exists [24].

A strong correlation between increasing temperature and increased oxidation has been found for all ferritic-martensitic steels [25]. Using HCM12A as an example, the effect of temperature and time on the growth of oxide on ferritic-martensitic steels can be seen in Figure 2.6 and 2.7 [80]. At 500℃ and 600℃, the growth of the oxide roughly follows parabolic kinetics and the exponent is about 0.4 for this material in these tests. At temperature below the critical point, very little oxide growth can be observed even up to 1026 h. The growth of oxide increases significantly with the increasing of SCW temperature from 350℃ to 600℃. The activation energies of the oxidation of T91, HCM12A and HT9 in SCW at temperatures ranging from 400℃ to 600℃ have been estimated to be 189, 177 and 172 kJ/mol, respectively [104].

Extensive experiments conducted by Graham and Hussey [26] have suggested that for Ni, Cr, Fe, and Fe-Cr alloys, the outer oxides grow predominantly by outward diffusion of cations. In particular, the activation energy for the diffusion of iron in Fe_3O_4 is 230 kJ/mol, for nickel in NiO the value is 234 kJ/ mol, and for chromium in Cr_2O_3, the value is 420 kJ/mol [32]. The activation energy for diffusion of oxygen in Fe_2O_3 is 610 kJ/mol [31], and that for Fe_3O_4 is considerably small. However, the diffusion coefficients cannot account for the measured oxide thickness. Nevertheless, evident results suggest that the inner oxide layer grows by the inward diffusion of oxygen. The diffusion through short-circuit paths, such as pores, cracks and grain boundaries, accounts for the high oxidation rates observed.

According to the results showed in Figure 2.6, for the time range up to 1026 hours, the oxide scales developed on ferritic-martensitic steels are stable, and could maintain a constant average density, and do not spall from the surface [106]. The weight gain data showed in Fig. 2.6 are proportional to the oxide thickness. The oxide density is greater for samples exposed to SCW with high oxygen concentration (2000 ppb) rather than samples exposed to SCW with low dissolved oxygen concentration (25ppb). Plan view and cross-sectional images of the oxides do not show any spallation [106].

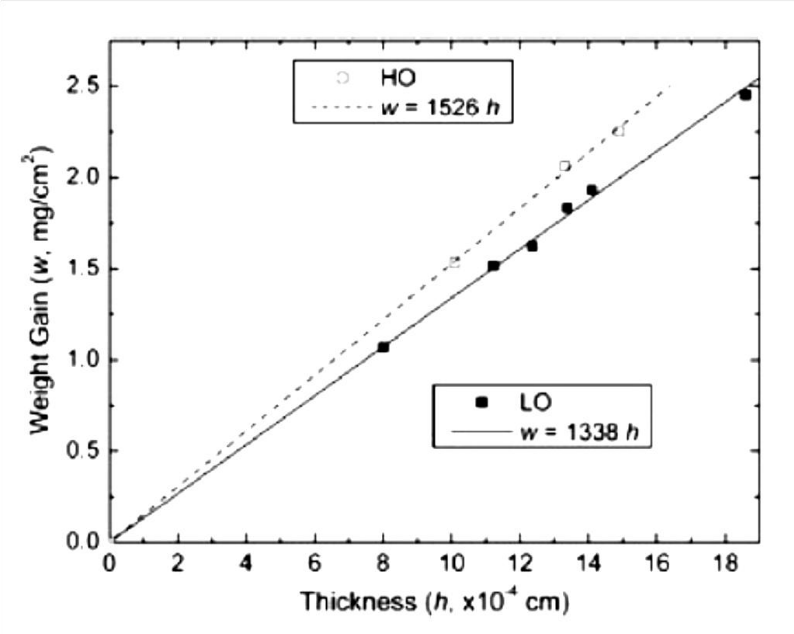

Figure 2.6 *- Weight gain as a function of oxide thickness for HCM12A exposed to 25 ppb and 2000 ppb oxygen at 500 ℃ [106].*

The oxide growth rate and associated weight gain of ferritic-martensitic steels are correlated to the dissolved oxygen concentration as shown in Figure 2.7 [104] which shows the corrosion of alloy HCM12A in SCW. For oxygen concentration from 10 ppb to 300 ppb, the weight gain which indicates the oxide growth, decreases slightly with the increase of dissolved oxygen concentration. However, the weight gain experiences a sharply increase when the oxygen concentration goes up to 2000 ppb, due to the enhanced oxidation. In addition, the formation of a hematite layer formed over the outer layer at the higher dissolved oxygen content supercritical water also plays an important role in the significant weight gain increase observed on samples exposed to 2000 ppb dissolved oxygen supercritical water. No significant hematite crystal has been found for the tests with 10-300 ppb dissolved oxygen, in which case the oxidation was the slowest [37].

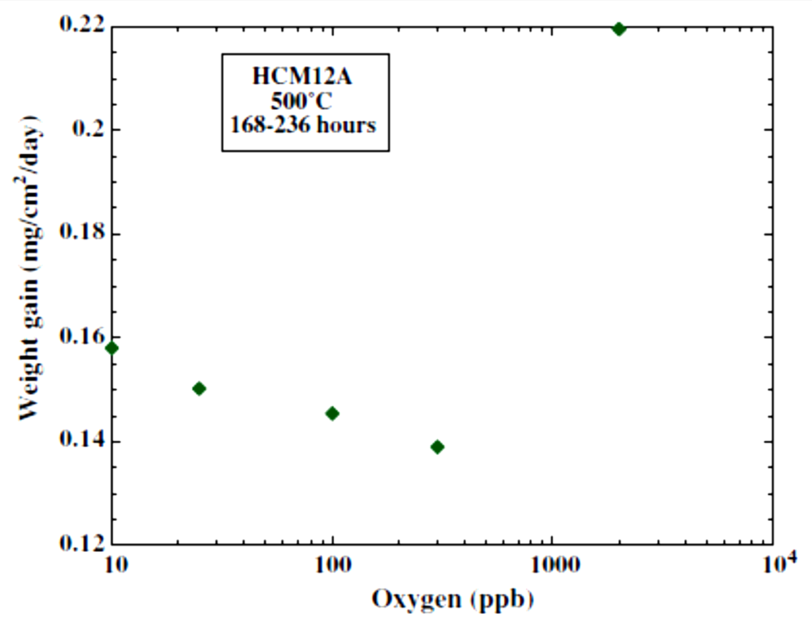

Figure 2.7 *- Weight gain as a function of temperature for HCM12A exposed to low oxygen concentration supercritical water for 1026 hours [104].*

For conventional ferritic-martensitic steels, increasing the bulk chromium concentration reduces the weight gain due to oxidation. An example of this correlation is shown in Fig. 2.8 where the 9 at.% Cr alloy NF616 has a greater weight gain than the 12 at.% alloy HCM12A [104]. The same trend is seen in the weight gain data for T91 (9Cr) and HT9 (12Cr) for all temperatures and times evaluated [130]. The results obtained by Cho and Kimura [16, 25], as well as Jang

[39] who tested ferritic-martensitic steels over a range of Cr content, also show that increasing Cr content led to the decrease of weight gain. However, different corrosion behavior was observed in oxide dispersion strengthened ferritic-martensitic steels. It has been found that the JAEA 9Cr ODS alloy shows the lowest weight gain of all the tested ferritic-martensitic steels presented in Figure 2.8 [108].

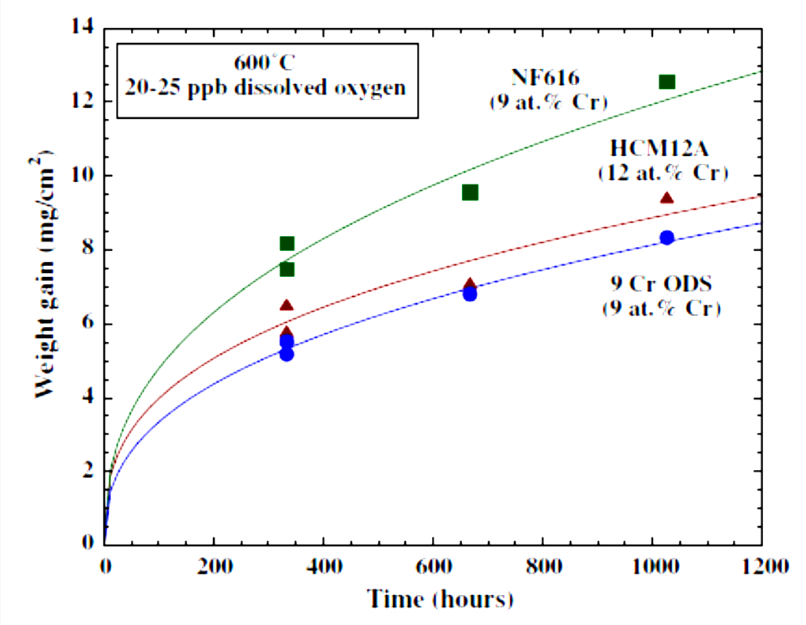

Figure 2.8 *- Weight gain as a function of time for NF616, HCM12A, and 9Cr ODS exposed to low oxygen concentration supercritical water at 600 ℃ [108].*

2.2.2 Austenitic steels

Austenitic steels were selected as one of the candidate materials for supercritical water reactor systems because of their good corrosion resistance and relative high radiation resistance compared to Ni-based alloys. So far, the following austenitic steels have been investigated by international programs: 304L, 304, 304H, 316L, 316, 310S, D9 and 800H.

Most results of SCW corrosion tests for austenitic steels show that the oxide scale formed consists of a two- or three-layer structure, similar to the oxide scales formed in air, vacuum and subcritical water [57-59]. The outer oxide layer generally consists of magnetite, and inner oxide layer is rich in chromium and consists of either an iron-chromium spinel or an iron chromium oxide with a hematite structure [11, 50, 59]. As in the case of ferritic-martensitic steels, an internal oxidation layer is also observed between the inner oxide layer and the base metal. It is evidenced by a gradually decreasing oxygen diffusion profile in this transition zone.

A typical structure and composition profile for an oxide scale grown on austenitic steel (800H) is shown in Figure 2.9 [30]. The oxide structure is somewhat similar to those formed in ferritic-martensitic steels, except that the outer oxide layer is composed of both magnetite and hematite.

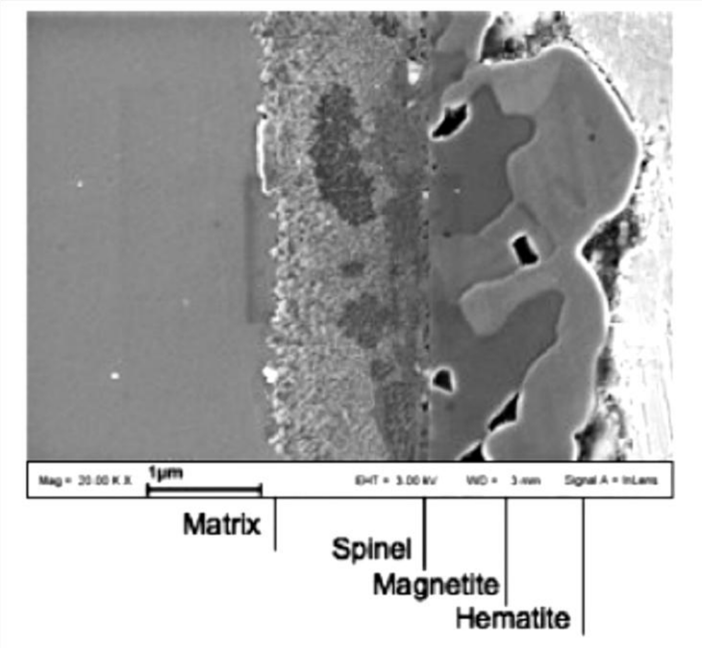

Figure 2.9 *- Cross-section of oxide formed on Alloy 800H exposed to 500 ℃ SCW with 25 ppb dissolved oxygen concentration for 505 hours [30].*

An additional difference between austenitic and ferritic-martensitic steels is the adherence of the outer oxide layer. In many of the austenitic stainless steels with higher bulk concentrations of nickel and chromium, the outer oxide layer has a tendency to spall, as demonstrated in the plan-view images from D9 exposed to SCW at 500 ℃ with a dissolved concentration of 2000 ppb as shown in Figure 2.10 [60].

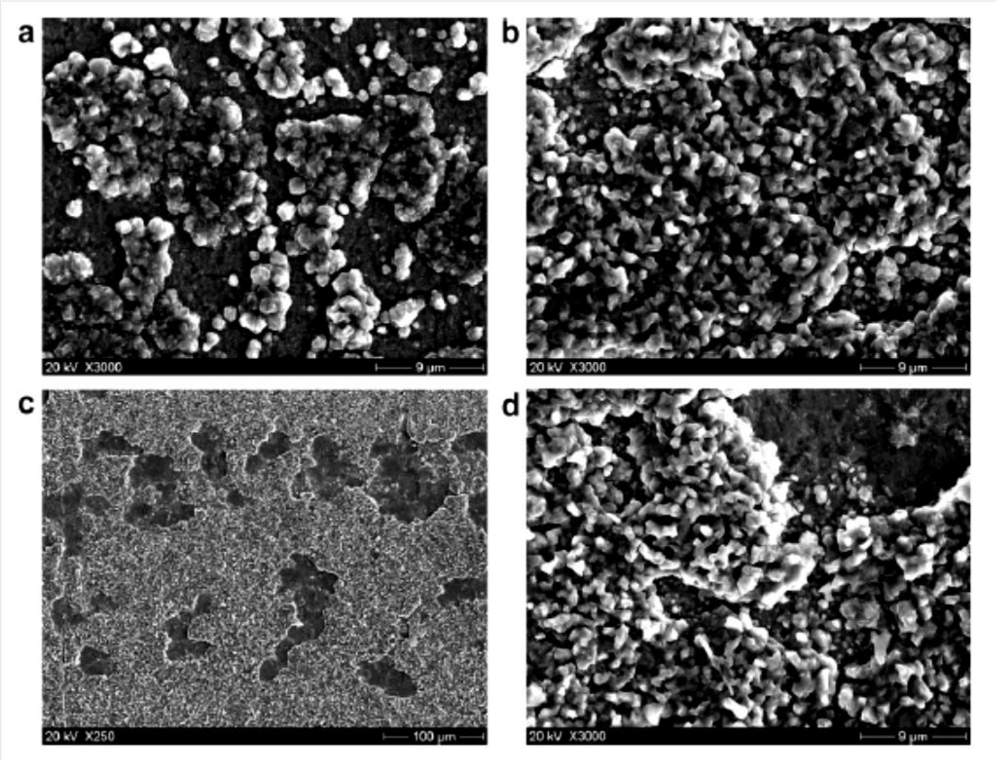

Figure 2.10 *- SEM surface morphologies of the D9 samples after exposure to 2000 ppb SCW at 500 ℃ for (a) 168 hours, (b) 335 hours and (c, d) 503 hours [60].*

Austenitic stainless steels usually showed a smaller weight gain than ferritic-martensitic steels [11,13,56]. An example of typical kinetics for tests to 1026 h is shown in Figure 2.11 for alloy D9. For 500 ℃ and 600 ℃, the oxide kinetics appears parabolic, but the data scatter is greater in austenitic alloys than in ferritic-martensitic steels. In some austenitic alloys, a portion of this scatter is attributed to spallation. The oxidation rate in austenitic alloys is smaller than in ferritic-martensitic alloys. The relation between oxidation rate and temperature is similar with ferritic-martensitic steels. The oxidation rate of austenitic steels increases dramatically with increasing temperature. Activation energy has been calculated for some austenitic steels, specifically 210 kJ/mol for 304L and 214 kJ/mol for 316L, higher than the energy measured in T91, HCM12A, and HT9 [104].

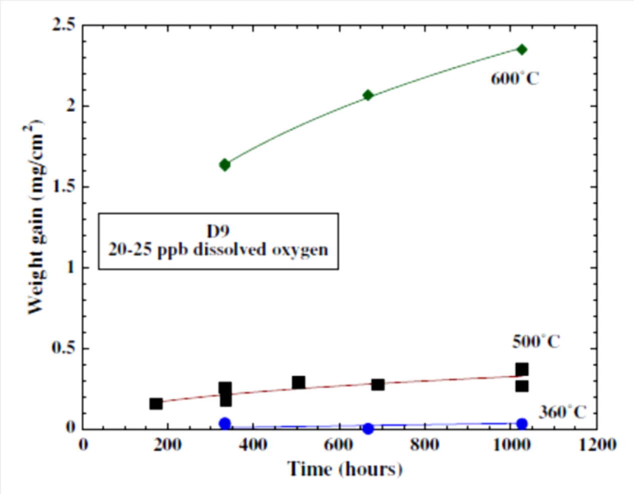

Figure 2.11 *- Weight gain as a function of time for D9 exposed to low oxygen concentration supercritical water at 360 ℃, 500 ℃ and 600 ℃ [41].*

The effect of dissolved oxygen is not straightforward for austenitic alloys as that for ferritic-martensitic steels. This is illustrated in Figure 2.12 for D9 and Figure 2.13 for 316 and 316L [43].

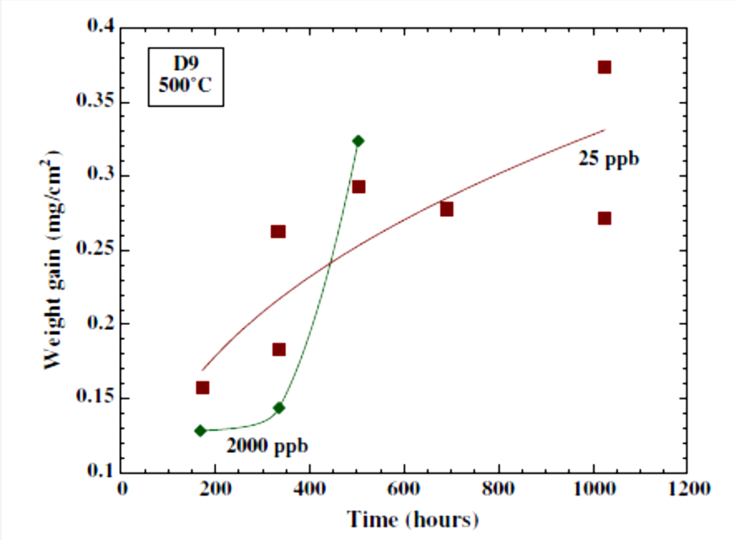

Figure 2.12 *- Weight gain as a function of time for D9 exposed to 25 ppb and 2000 ppb oxygen concentration at 500 ℃ [43].*

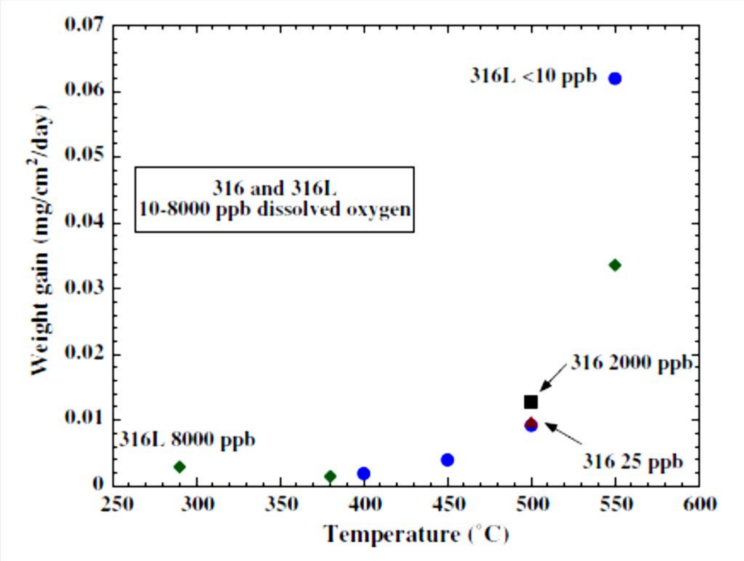

Figure 2.13 *- Weight gain rate as a function of temperature for 316L exposed in < 10 ppb dissolved oxygen (blue circles), 316L exposed in 8000 ppb dissolved oxygen (green diamonds), 316 exposed in 25 ppb dissolved oxygen (red triangles), and 316 exposed in 2000 ppb dissolved oxygen (black squares) [41,43].*

For D9 exposed at 500 ℃, at short times, the weight gain is smaller at very high (2000 ppb) dissolved oxygen than at low (25 ppb dissolved oxygen). At longer times (between 333 and 505 h), the oxidation rate of the D9 exposed to 2000 ppb dissolved oxygen increases significantly. It is noted for the D9 samples exposed to 25 ppb oxygen content, particularly for longer exposure times that the weight gain remains nearly constant, which may be attributed to oxide spallation in these alloys. The weight loss due to spallation counterbalances the weight gain due to the growth of the oxide layer [3]. Weight gain rate for 316 and 316L as a function of temperature from this work is compared to that of Kasahara et al. [23], who exposed 316L in a static autoclave at 8000 ppb dissolved oxygen, in Figure 2.13. At low temperatures, the oxidation is minimal and no significant difference is noted between 316 and 316L or between exposures at different oxygen concentration. At 500 ℃, higher dissolved oxygen leads to greater weight gain in 316. At 550 ℃, the weight gain rate is actually higher for the deoxygenated (<10 ppb) case than for the 8000 ppb case. Therefore, the effect of oxygen is not as straightforward in the austenitic steels as was seen in the ferritic-martensitic steels and more study is needed to identify the optimal oxygen concentration to minimize corrosion.

The trends in weight gain as a function of time for three austenitic alloys exposed to 20－25 ppb dissolved oxygen are shown in Figure 2.14. The weight gain is always the smallest for 800H, but the fluctuations in weight gain were observed indicating the oxide spallation that may occur for this alloy. The relative weight gain of 316 and D9 differ as temperature varies. D9 has a greater weight gain at 500 ℃ and 316 has a greater weight gain at 600 ℃. The effect of bulk composition is not as straightforward in the austenitic steels as was seen in the ferritic-martensitic steels and greater study is needed to identify optimal alloying concentrations required to form thin stable oxides [3].

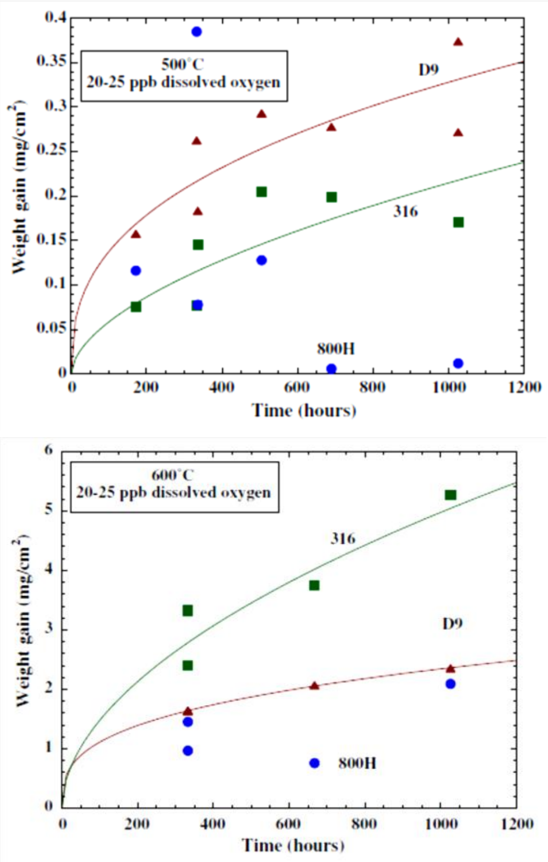

Figure 2.14 *- Weight gain as a function of time for D9, 316, 800H exposed to low oxygen concentration supercritical water as 500 ℃ and 600 ℃ [3].*

2.3 Corrosion Control Methods

As mentioned before, the water rod wall for the SCWR is as thin as about 0.5mm. After only 1000 hours exposure in SCW at 600℃, the thickness of the oxide scale grown on HCM12A is approximately 65μm, about 14% of the thickness of the water rod wall. So the oxidation should be reduced for ferritic-martensitic steels to make it acceptable for the application in a SCWR.

One method to improve the corrosion resistance is using ODS alloy as shown in Figure 2.8. The ODS steels show lower oxidation than conventional ferritic-martensitic steels. There increased corrosion resistance of ODS steels can be attributed to the two aspects. First, ODS steels include nanometer sized Y-Ti-O particles which are added for strengthening. After supercritical water exposure, ODS steels has a much deeper internal oxide layer. Thus the net conversion of metal to spinel appears to be driven by oxygen diffusion into the metal rather than cation diffusion to the oxide surface. Detailed microscopy indicates that the formation of Y-Cr-rich oxides along grain boundaries in the steel near the metal-oxide interface may block the cation diffusion [16]. As the inner spinel layer formed on ODS alloy is thinner, more porous and density lower, a smaller weight gain in ODS steels is observed. Second, the grain sizes of ODS steels are smaller than conventional ferritic-martensitic steels. The increased diffusion length may slow oxidation.

The other promising method to slow the oxidation of ferritic-martensitic steels in supercritical water is surface modification, including composition modification and grain size refinement. For surface composition modification, both oxygen and yttrium have been implanted into the surface of various ferritic-martensitic steels.

The weight gain changes of tested ferritic-martensitic steels with various surface implantation conditions are shown in Figure 2.15 [3].

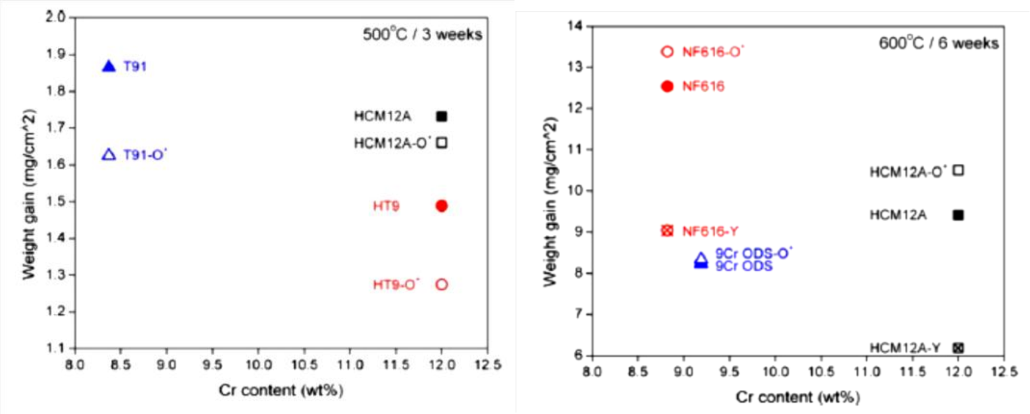

Figure 2.15 *- Effect of oxygen and yttrium surface implantation at 500 ℃, and 600 ℃ on T91, HCM12A, HT9, NF616, and 9Cr ODS [3].*

At 500℃, oxygen implantation reduced the weight gain in HCM12A, HT9, and T91**[3]**. Associated with the reduction in oxide thickness in HT9, a change in the oxide texture is observed early in the development of the oxide, but after longer time exposure, the texture are similar between samples with and without oxygen pre-implantation [67]. One possible explanation for the texture is that bombardment with oxygen ions may increase nucleation sites with certain preferred orientations at the initial stage of oxide formation, resulting in a denser textured oxide layer. Another possibile reason is that, among randomly orientated initial grains, some with certain crystal orientations grow faster than the others to release the stress introduced by the ion implantation. At 600℃, the oxygen pre-implantation is not an effective method to reduce the oxidation in supercritical water, but yttrium strongly reduced the oxidation rate in both NF616 and HCM12A. It has been proved that a thin layer of yttrium incorporated into the magnetite layer could reduce the oxidation by approximately 50% [50].

Grain refinement is considered as a promising approach to control the corrosion of ferritic-martensitic steels. Grain boundaries are regarded as ‘‘short-circuit’’ paths for the diffusion of elements, and hence play an important role in the oxidation/corrosion performance of materials. Grain refinement can lead to enhanced diffusion of elements from the bulk to the surface since the diffusion coefficient along GBs can be several orders of magnitude higher than that in the bulk lattice [61, 70]. This can also promote a quicker formation and self-healing of protective oxide scales [48]. Studies on nanocrystallized 304 stainless steel oxidized in air with 0–40% water vapor in the temperature range of 700 to 900℃, showed no breakaway oxidation, whereas in coarse-grained samples of the same material, breakaway oxidation was observed [39]. This improvement was attributed to sufficient outward diffusion of chromium through an abundance of GBs in the nanocrystallized samples that resulted in the formation of a protective Cr-rich oxide layer rather than a non-protective Fe-rich oxide layer.

According to the approaching method and affected area, grain refinement can be divided into two categories, general grain refinement and surface grain refinement. General grain refinement is usually achieved by cold work and heat treatment, by which the whole material will be grain refined. For the surface grain refinement, which usually approached by shot peening or ultrasonic peening, only the surface of the material will be grain refined and the depth of the fine grain layer is usually about 100 μm. Y. Tsuchiya, etc. have investigated the effect of general grain refinement on corrosion behavior of austenitic steels in subcritical and supercritical water [24]. The time dependency of the weight change of the austenitic stainless steel at 550oC in SCW is shown in Figure 2.16. The weight of Type 316L SS and Type 304L SS increased when the duration time exceeds to around 400 hours. The weight changes of Type 310S, fine grain 304L SS and fine grain 310S SS were remarkably smaller than those of Type 316L SS and Type 304L SS. It is found that the influence of Cr content and grain size becomes remarkable at 550^{o}C. The corrosion rates of the austenitic stainless steels at 550oC are shown in Figure 2.17. The corrosion rate decreased in the order of Type 304L SS>Type 316L SS >>Type 310S SS>> fine grain 304L SS> fine grain 310S SS. Comparing the oxidization and release, Type 316L SS and Type 304L SS were dominated by oxidation, and Type 310S SS has a larger rate of oxidation with a noticeable amount of dissolution. The comparison of the corrosion rate of normal grain with fine grain austenitic stainless steel indicates the fine grain material has remarkably lower corrosion rate. Thus, the improvement of corrosion resistance at 550°C was realized by means of the grain refinement.

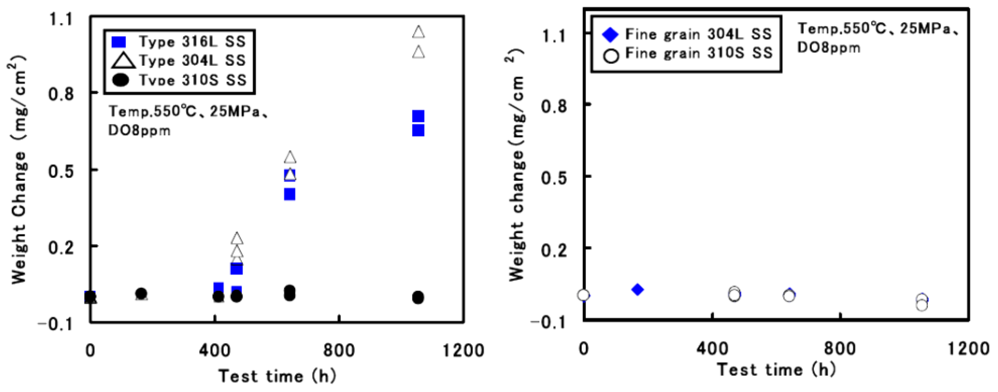

(a) Type 316L SS, Type 304L SS and Type 310S SS

(b) Fine grain 304L SS and 310S SS

Figure 2.16 *- Time dependency of weight change of austenitic steels at 550 ℃ [83].*

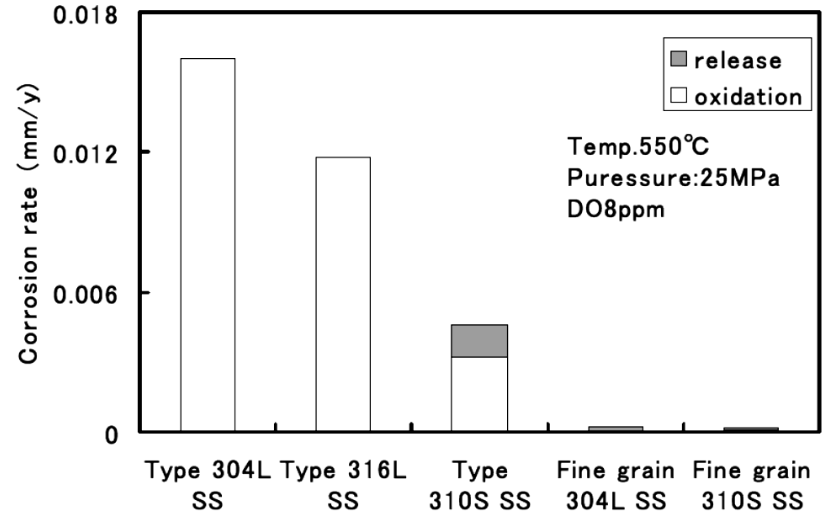

Figure 2.17 *- Corrosion rates of austenitic steels at 550 ℃ [83].*

2.4 Surface Grain Refinement

Actually, the majority of failures of engineering materials are very sensitive to the structure and properties of the material surface, and in most cases material corrosion and failures occur on the surface. Therefore, optimization of the surface structure and properties may effectively enhance the global behavior of materials. Surface grain refinement is one of the promising methods to control the corrosion in supercritical water.

2.4.1 Shot Peening

Shot peening as one of the surface grain refinement methods has been proved to be effective to improve the corrosion resistance of ferritic-martensitic steels in supercritical water [22]. Ren et al. have investigated the corrosion behavior of grain refined commercial F/M steels and binary model alloys in SCW with 25 ppb dissolved oxygen at 500 ^{o}C for up to 3000 h. Improved corrosion resistance was observed for the sampes after grain refinement, which attributed to the formation of a Cr-rich or chromium oxide layer facilitated by the enhanced diffusion of chromium through dense GBs produced by grain refinement. Shot Peening also reduced the critical chromium content to form a continued chromium oxide layer from about 18 wt% in the as-received condition to about 15 wt% in the Fe-Cr model alloys. It can be seen that the grain refinement effect becomes more evident with increasing chromium contents and the worst case was observed in NF616 which has the lowest chromium concentration. The inner spinel compound layer was found to be more effective to increase the corrosion resistance with increasing chromium content because its structure is more ordered with chromium resulting in a lower diffusivity [16]. By shot peening, both outward diffusion of chromium and iron are enhanced through abundant GBs, and therefore the chromium content in the base steel has to be high enough to form an effective diffusion barrier layer. Otherwise, the enhanced diffusion of iron will be deleterious to the corrosion resistance of shot-peened samples, as observed in NF616. In the shot-peened NF616, chromium content is higher in the inner oxide layer (~14 at%) compared to the as-received sample (~8 at%), but it is still not as high as the shot-peened HT9 (~18 at%),. Other minor elements in these commercial steels may have considerable influence on grain refinement effects in certain cases. T91, another 9Cr F/M steel only has a slightly higher chromium content than NF616, shows a significant improvement in corrosion resistance by grain refinement. This probably caused by the higher silicon content in T91 than that in NF616 and silicon can facilitate the diffusion of chromium [27]. The grain refinement effect is also influenced by exposure Time. The improvements of corrosion resistance become more evident after long-time exposure and appear saturated after 1700 hours.

2.4.2 Ultrasonic Peening

2.4.2.1 History

The following is a summary of a more detailed historical review of ultrasonic peening based on the review given by Kudryavtsev et al. and other literatures[74] . Research on ultrasonic treatment of metals started in the 1950s in the U.S.A., Austria and the former Soviet Union. This research was rather theoretical and mainly concentrated on demonstrating the beneficial effect of ultrasound on ductility and strength properties of metals. At the same time first attempts were made to improve the geometry of welded joints through deformation treatment employing ultrasound. However, these attempts showed little success. The main problem lay in the design of the equipment for ultrasonic treatment. In the 1960s and 70s, advances in equipment design were achieved in the U.S.A. and the former Soviet Union. Intensive investigations were especially carried out at the Institute for Metal Physics (IMP) in Kiev, developed the still employed intermediate element-striker technology (see next section). With the technology at hand, the IMP started to focus on improving the fatigue behavior of welds, but due to political boundaries these findings were mainly kept to the Eastern European scientific and industrial world. Only after the fall of Communism, the benefits of weld improvement treatment by ultrasonic peening became better known in the West, leading to close cooperation between the IMP and the

Western industry. Presently, the research mainly concentrates on developing optimal and user friendly applications of ultrasonic peening for the industry, employing expert systems [65].

2.4.2.2 Mechanism

In ultrasonic peening the strikers (hammer or needles) are activated by a transducer. In the early models of ultrasonic peener the strikers were directly attached to the transducer, resulting in uneconomical use of the ultrasonic energy and difficult handling of the tool. The development of the intermediate element-striker technology allowed for a much more optimal use of the ultrasonic energy. This technology is still state of the art and is explained in the following [71, 74]. The two basic tools for ultrasonic peening consist of a generator and a transducer as shown in Figure 2.18. The generator supplies the electrical energy, which is converted into ultrasonic vibrations by either a magnetostrictive or piezoelectric transducer. Magnetostrictive transducers use the property of certain materials to expand and contract when placed under changing magnetic fields. First, the ultrasonic energy from the generator has to be transformed into an alternating magnetic field through the use of a wire coil. Resonant strips of the magnetostrictive material are then used to induce the desired vibrations.

Piezoelectric transducers use a similar principle by changing the dimensions of a material susceptible to electrical charge. Since the electric energy is directly transformed into ultrasonic vibrations, piezoelectric transducers are more efficient than magnetostrictive transducers, which require dual energy conversion from electric to magnetic to ultrasonic. The efficiency of modern piezoelectric transducers is over 95% compared to roughly 35% for typical magnetostrictive transducers. Furthermore, magnetostrictive transducers are normally heavier due to their need for a water cooling system. Therefore, piezoelectric transducers are more commonly used today [72].

Modern transducers employ the intermediate element-striker technology. Figure 2.19 shows a schematic section through an ultrasonic tool [76]. The forced oscillation of the ultrasonic transducer (1) is transferred to a concentrator of oscillating velocity, called waveguide (2). The output end of the waveguide impacts upon the strikers (3), which are not connected to the transducer (1) and thus free to move. At the output end of the waveguide the ultrasonic oscillation (A) is transformed to impacts (B), which indent the work piece (4). A complex interaction between the waveguide, the strikers, and the work piece results in a superposition of non-periodic stress pulses and ultrasonic periodic stress waves in the work piece.

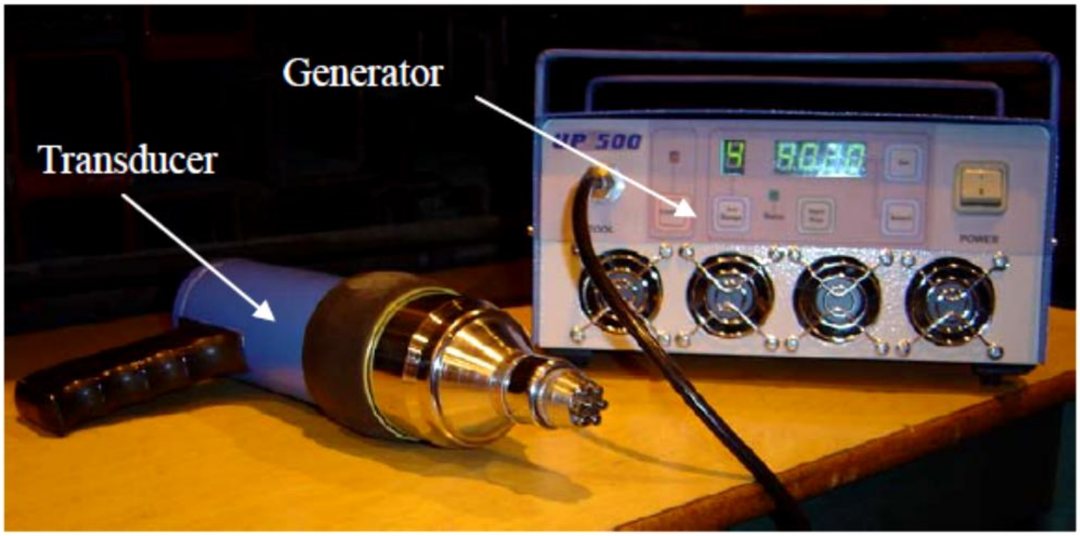

Figure 2.18 *- Ultrasonic generator and transducer.*

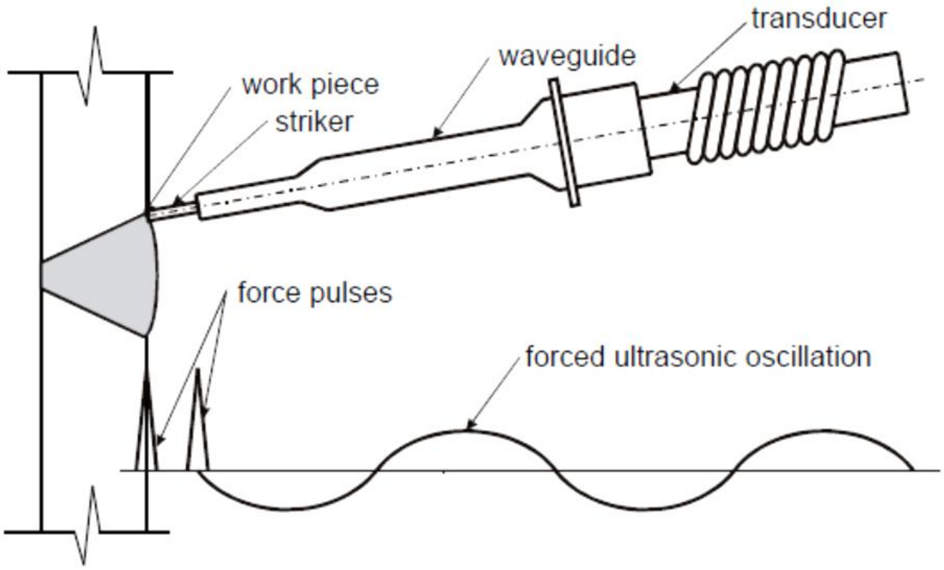

Figure 2.19 *- Mechanism of ultrasonic peening [76]*

2.4.2.3 Application

Most of the applications of ultrasonic peening are focus on improving the fatigue performance so far. However, as the effect is similar with shot peening, ultrasonic peening has been investigated to control the corrosion of some austenitic steels. According to the research from Korean and Ukraine, it is effective to use ultrasonic peening to improve the corrosion resistance of AISI 304 and AISI 321 stainless steels in room temperature [78]. However the corrosion tests in their study were potentiodynamic polarization measurements in 0.5 M H2SO4 at room temperature and cyclic potentiodynamic polarization measurements taken in 3.5 wt.% NaCl at room temperature. The conditions are quite different from that in supercritical water. For the effect of ultrasonic peening on corrosion behavior of stainless steels or alloy, very little data can be found nowadays. More study is still needed to study this promising corrosion control method for improving the corrosion resistance in supercritical water.

Chapter 3

Experimental

3.1 Materials and Preparation

In order to investigate the corrosion behavior of ferritic-martensitic steels in supercritical water, five kinds of ferritic-martensitic steels with different additions of Si and Mn have been designed and fabricated. The adding of Si and Mn is aiming to investigate the effect of alloy elements Si and Mn on the corrosion of F-M steels in SCW. Table 3.1 lists the chemical compositions of these steels. These five kinds of steels have been denoted as FM1, FM2, FM3, FM4 and FM5 in order to describe easily. FM1, FM2 and FM5 have been designed for study of the Si content on the corrosion, because they have very similar Cr, Mn and Fe contents and the Si content increases from 0.6 wt. % to 2.2 wt.%. FM5, FM3 and FM4 have been designed to investigate the effect of Mn content on the corrosion, in which the content of Mn increases from 0.6 wt. % to 1.8 wt. % with little variation of other element contents.

***Table 3.1** - Chemical composition of five kinds of ferritic-martensitic steels*

Material	Alloy element (wt. %)			
	Cr	Si	Mn	Fe
FM.1	11.1	0.7	0.6	Balance
FM.2	11.2	0.7	1.1	Balance
FM.3	11.6	1.1	1.8	balance
FM.4	11.6	2.2	1.7	Balance
FM.5	11.7	0.6	1.8	Balance

3.2 Specimen Preparation

Samples with dimensions of 20mm×5mm×2mm was cut from the five kinds of F-M steels. The samples were ground using sand paper from 240# to 1200# grit finish. The samples were ultrasonic cleaned in acetone for 30 minutes. After complete drying, the samples were divided into two groups. Samples in Group 1 were named as P-FM-1 to P-FM-5, while samples in Group 2 were named as NP-FM-1 to NP-FM-5. Then ultrasonic peening treatment was applied on all samples in Group 1. The peening facility used for the surface treatment is a set of HJ-III Ultrasonic Peening Treatment Equipment from Sunbow Technology. The main parameters of ultrasonic peening treatment are shown in Table 3.2.

Table 3.2 *- Main parameters of ultrasonic peening treatment*

Parameter	**Value**
Work frequency	20 kHz
Work load	10 g
Time	180 s
Impact needle diameter	4 mm

However, the peening treatment was applied only on the 20mm×5mm sides of samples in Group 1, the 20mm×2mm and 5mm×2mm sides were too small to peen on them. After ultrasonic peening treatment, samples in Group 1 were cleaned with acetone in ultrasonic water bath for 30 minutes.

The information of all the samples used for supercritical water exposure is given in Table 3.3.

Table 3.3 *- The main parameters of samples used for supercritical water exposure.*

Name	Size	Surface treatment	Alloy element (wt%)			
			Cr	Si	Mn	Fe
P-FM-1	20mm× 5mm× 2mm	Ultrasonic peened surface	11.1	0.7	0.6	Balance
P-FM-2			11.2	0.7	1.1	Balance
P-FM-3			11.6	1.1	1.8	balance
P-FM-4			11.6	2.2	1.7	Balance
P-FM-5			11.7	0.6	1.8	Balance
UP-FM-1	20mm× 5mm× 2mm	Polished surface (up to 1200# grit)	11.1	0.7	0.6	Balance
UP-FM-2			11.2	0.7	1.1	Balance
UP-FM-3			11.6	1.1	1.8	balance
UP-FM-4			11.6	2.2	1.7	Balance
UP-FM-5			11.7	0.6	1.8	Balance

3.3 Corrosion exposure in supercritical water

3.3.1 Test Setup

All the supercritical water exposure tests were conducted using a static capsule autoclave as shown in Figure 3.1. The capsule was made of 316L stainless steel tube with a length of 10 cm. The outer diameter of the tube is 9mm and the inner diameter is 6mm. The inner wall was polished using sandpaper up to 1200# grit and then ultrasonic rinsed in acetone for 30 minutes. Then the samples were placed inside the tubes, and certain amount of DI water or water solution with 5% H_2O_2 was filled into theses tubes. After filling water, the tubes were sealed by two caps made of 316L stainless steel. All the tubes and caps used in the tests were fabricated by Swagelok Company. Then the sealed capsules were put into a furnace heated to 500℃ for different exposure time. As there was certain amount of water sealed in the capsules, and the volume in the capsule is constant during the test, so when the capsules were heated, the environment inside the tube would reach to designed supercritical water conditions.

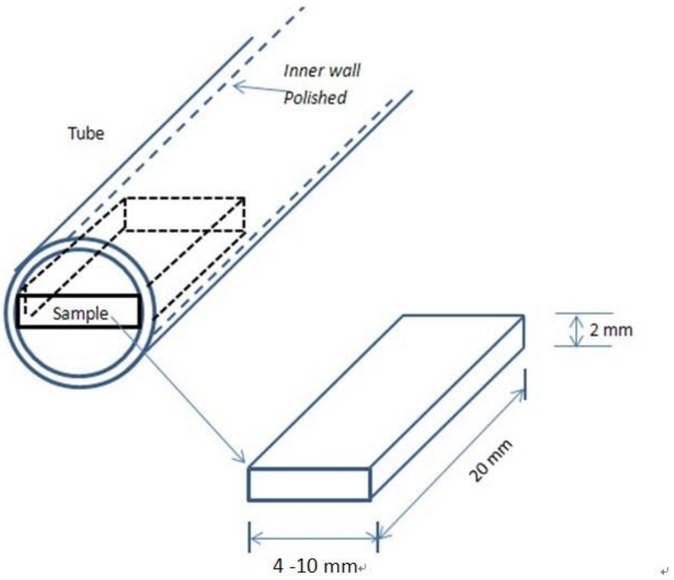

Figure 3.1 *- Tube and coupon sample used for supercritical water test.*

3.3.2 Test Conditions

Table 3.3 lists the conditions of the supercritical water tests. Test 1 and Test 2 have been conducted for all the samples in Group 1 and Group 2. For each test condition, 3 specimens for each kind of material were tested in order to ensure the results were valid.

Table 3.4 *- The conditions of the supercritical water tests.*

	T and P	**Oxygen content**	**Exposure time**
Test 1	500℃ 25MPa	8 ppm	100 h, 250 h, 500 h, 1000 h
Test 2	500℃ 25MPa	5% H_2O_2 added	100 h, 250 h, 500 h, 1000 h

3.3.3 Characterizations

After supercritical water exposure, capsules were taken out from furnace and cooled to room temperature. Then coupons were taken out from capsules, cleaned, dried. The weights of samples were measured. The surface morphology and cross-section of samples after exposure were characterized by XRD, SEM and EDS.

A scanning electron microscope (SEM) is a type of electron microscope that produces images of a sample by scanning it with a focused beam of electrons. The electrons interact with electrons in the sample, producing various signals that can be detected and reveal the information about the sample's surface topography and composition. The electron beam is generally scanned in a raster scan pattern, and the beam's position is combined with the detected signal to produce an image. The types of signals produced by a SEM include secondary electrons (SE), back-scattered electrons (BSE), characteristic X-rays, light (cathodoluminescence) (CL), specimen current and transmitted electrons. Back-scattered electrons (BSE) are beam electrons that are reflected from the sample by elastic scattering. BSE are often used in analytical SEM along with the spectra made from the characteristic X-rays, because the intensity of the BSE signal is strongly related to the atomic number (Z) of the specimen. BSE images can provide information about the distribution of different elements in the sample. Characteristic X-rays are emitted when the electron beam removes an inner shell electron from the sample, causing a higher-energy electron to fill the shell and release energy. These characteristic X-rays are used to identify the composition and measure the abundance of elements in the sample [136].

Energy-dispersive X-ray spectroscopy (EDS, EDX, or XEDS) is an analytical technique used for the elemental analysis or chemical characterization of materials. It relies on the investigation of an interaction of some source of X-ray excitation. Its characterization capabilities are due to large part of the fundamental principle that each element has a unique atomic structure allowing unique set of peaks on its X-ray spectrum [137].

The furnace used for supercritical water exposure is a MTI OTF-1200X furnace, the maximum working temperature can be set up to 1200 ℃.The XRD system used in this study is a Rigaku Ultimate IV multipurpose X-ray diffraction system. The SEM system used in this study is Zeiss EVO MA 15 equipped with a Bruker Silicon Drift Detector for Energy Dispersive X-Ray analysis/ mapping with a peak resolution of 125 eV.

Chapter 4

Corrosion of Ferritic-Martensitic Steels in Supercritical Water

4.1 Introduction

This chapter presents the results of investigating the corrosion behavior of five kinds of ferritic-martensitic stainless steels in supercritical water. The oxidation kinetics occurred during the SCW exposure were studied. The oxide scale grown on the surface was characterized. The corrosion mechanism, especially the effect of minor alloy elements (Si, Mn), were discussed in this chapter.

4.2 Experimental

Table 4.1 lists the information of the samples examined in this chapter. Coupons with dimensions of 20mm×5mm×2mm were cut from the as-received alloys. The coupons were ground using sand paper from 240# up to 1200# grit finish and then were ultrasonically cleaned with acetone for 30 minutes. All the coupons were weighted by digital balance and the dimensions were measured by digital micrometer.

Table 4.1 *– Ferritic-martensitic steels for SCW test.*

Name	Size	Surface treatment	Alloy element (wt%)			
			Cr	Si	Mn	Fe
UP-FM-1	20mm×5mm×2mm	Polished surface (up to 1200# grit)	11.1	0.7	0.6	Balance
UP-FM-2			11.2	0.7	1.1	Balance
UP-FM-3			11.6	1.1	1.8	balance
UP-FM-4			11.6	2.2	1.7	Balance
UP-FM-5			11.7	0.6	1.8	Balance

Supercritical water exposure tests were conducted in capsule autoclaves at 500℃, 25MPa with a dissolved oxygen concentration of 8ppm. The SCW exposure lasted from 100 hours to 1000 hours. The weight changes were measured after each test in order to investigate the oxidation kinetics. SEM, EDS and XRD were employed to characterize the oxide scales formed.

4.3 Results

4.3.1 Oxide kinetics

Figure 4.1 shows the weight changes of ferritic-martensitic steels as a function of exposure time (from 100 hours to 1000 hours) when exposed to supercritical water at 500 ℃ and 25MPa with 8ppm dissolved oxygen. A strong correlation can be found between increasing the exposure time and increasing the oxidation for all the ferritic-martensitic steels tested.

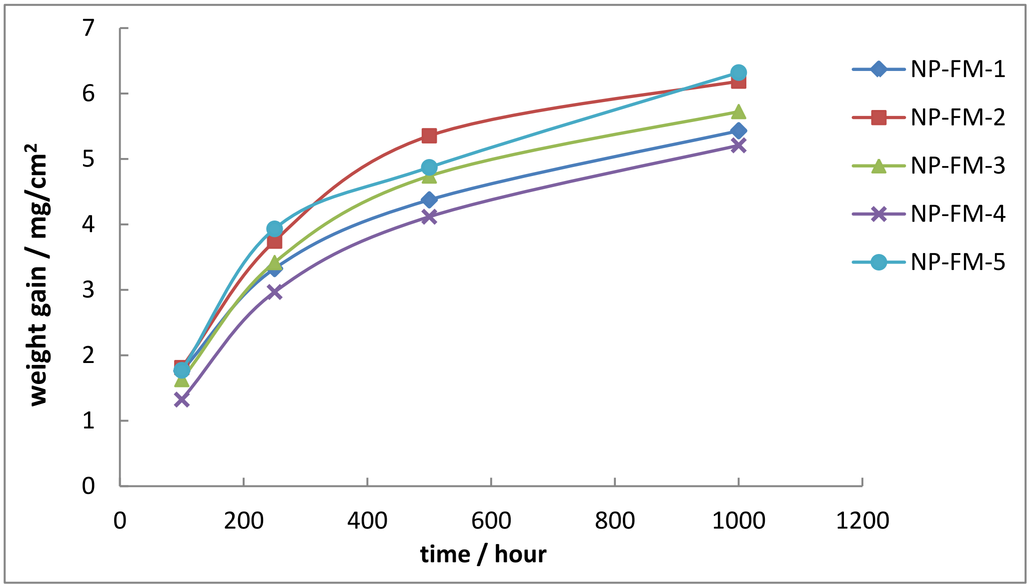

Figure 4.1 - *Weight change as a function of exposure time in 500 ℃ 25MPa supercritical water with 8ppm dissolved oxygen.*

As shown in Figure 4.1, weight gains increased with the exposure time for all the ferritic-martensitic steels tested in SCW from 100 hours to 1000 hours. After 1000 hours exposure, Sample UP-FM-4 showed the smallest weight gain which is about 5.208 mg/cm^2 and the Sample UP-FM-5 suffered more corrosion, as the highest weight gain about 6.32 mg/cm^2 was detected.

High temperature oxidation kinetics of metals or alloys is commonly controlled by the diffusion of cationic or anionic species through the oxide scale [1]. Such a controlling usually leads to a parabolic growth behavior described by the following equation:

$$(\frac{\Delta \mathrm{M}}{\mathrm{S}})^2 = \mathrm{A} + \mathrm{k_p t}$$

in which ΔM is the weight change in a unit of mg, k_p is the rate constant, expressed in $mg^2cm^{-2}h^{-2}$, and S is the area oxidation took place in cm^2, and t is the oxidation time. According to the calculation shown in Appendix 1, the oxidation behavior of all the tested ferritic-martensitic steels roughly followed the parabolic laws. Table 4.2 lists the parabolic rate constant determined for the five tested materials. Sample UP-FM-5 has the largest parabolic rate constant which is around 0.0326, indicating a more severe corrosion suffered. Sample UP-FM-4 exhibited higher corrosion resistance as smaller parabolic rate constant around 0.0238 was derived.

***Table 4.2** – parabolic rate constants*

Name	Surface treatment	Parabolic rate constant ($mg^2cm^{-2}h^{-2}$)
		8ppm dissolved oxygen
UP-FM-1	Polished surface (up to 1200# grit)	0.0240
UP-FM-2		0.0311
UP-FM-3		0.0270
UP-FM-4		0.0238
UP-FM-5		0.0324

4.3.2 Characterization of Oxide Scales

Figure 4.2 shows the surface morphologies found on specimens after 1000 hour exposure in supercritical water. Figure 4.2(e) shows the surface morphology of oxide scale formed on UP-FM-5, while the oxide scale formed on UP-FM-3 is quite similar to it. Figure 4.2(d) shows the surface morphology of oxide scale formed on UP-FM-4 which is quite similar to the surface morphologies of UP-FM-1 and UP-FM-2. It is obvious that the oxide scale formed on the surface of UP-FM-5 (Fig. 4-2 (e)) is not continues, whereas continues and uniform oxide scales has been found on other samples as shown in (Fig. 4-2 (d)). However, the oxide particles in both kinds of scales have similar grain size which is about 7~8μm.

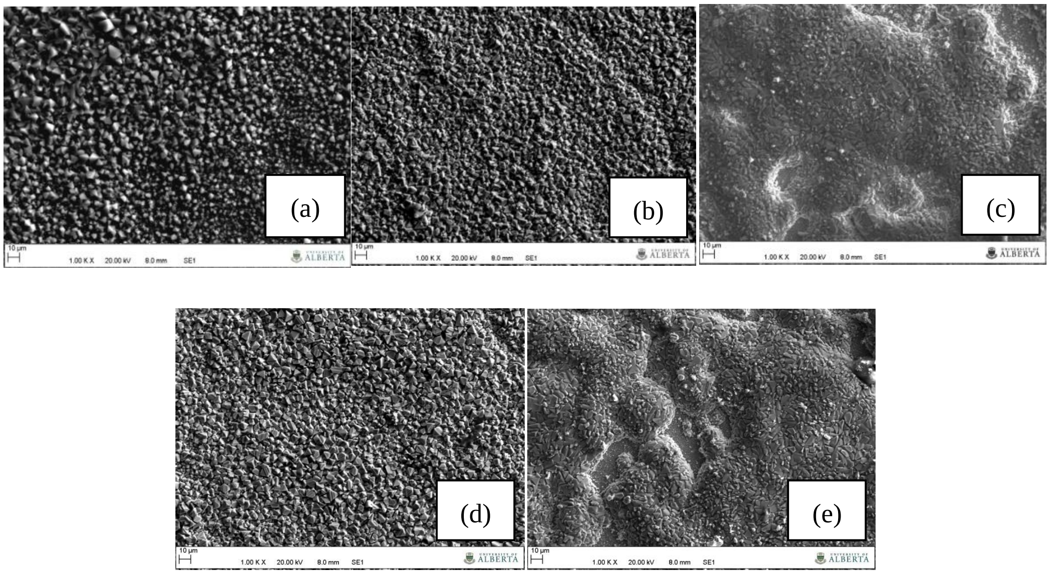

***Figure 4.2**- Surface morphology SEM images (1000×) after 1000 hour SCW exposure: (a) UP-FM-1, (b) UP-FM-2, (c) UP-FM-3, (d) UP-FM-4, (e) UP-FM-5 in low dissolved oxygen.*

Figure 4.3 shows the XRD result of the surface oxide scale formed on UP-FM-4 after 1000 hours supercritical water exposure. The oxide formed on the surface was identified to be magnetite. The oxides formed on the other four kinds of test material were found to be magnetite as well.

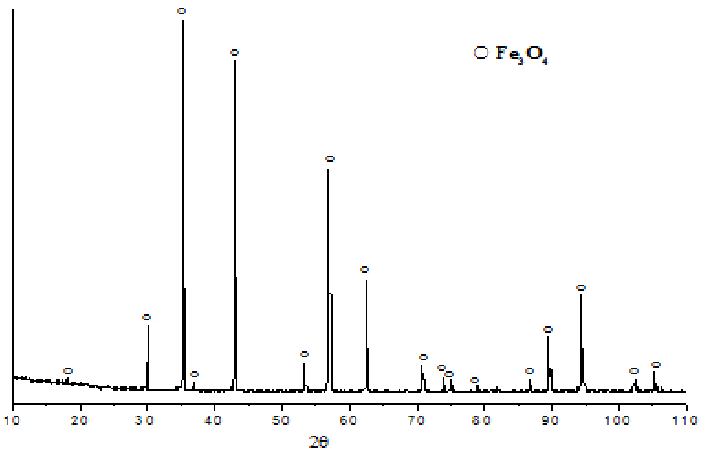

Figure 4.3 *- XRD result of the surface oxide scale formed on UP-FM-4 after 1000 hours supercritical water exposure.*

Figure 4.4 shows the cross-section SEM images of the oxide scales formed after 1000 hours supercritical water exposure. Distinct dual layer oxide scales were observed on all tested specimens after exposure. The outer layers consisting of the larger oxide grains appeared more porous than the inner layers that composed of much smaller oxide grains. However, the dual layer oxide scales formed on UP-FM-1, UP-FM-2, and UP-FM-4 seem more continuous and thinner than that formed on UP-FM-3 and UP-FM-5, which may be caused by the different Si and Mn contents.

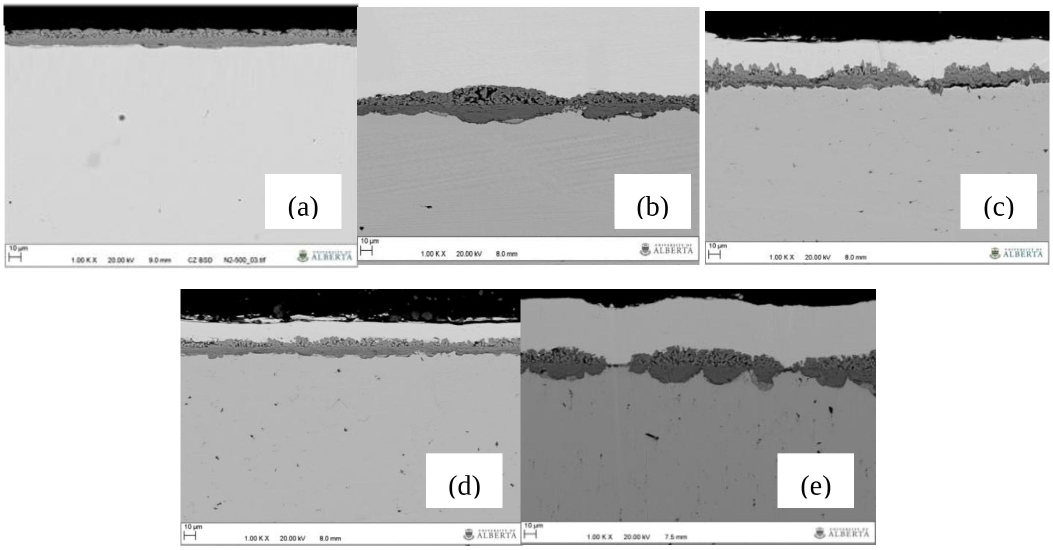

Figure 4.4 *- cross-section SEM images of (a) UP-FM-1, (b) UP-FM-2, (c) UP-FM-3 (d) UP-FM-4 and (e) UP-FM-5 after 1000 hour exposure in supercritical water with 8 ppm dissolved oxygen (1000×).*

Figure 4.5 shows the EDS mapping results of (a) UP-FM-4 and (b) UP-FM-5 as examples of the continuous and discontinuous oxide scales. According to the EDS mapping of UP-FM-4, the outer layer is predominately iron oxide whereas the inner layer shows significant chromium enrichment. Enrichment of silicon and manganese has also been found in the inner layer. The effect of the silicon and manganese enrichment will be discussed in Section 4.4.1. The outer layer is magnetite and the inner layer is iron-chromium spinel [3]. According to the EDS mapping data of UP-FM-5, the outer layer is predominately iron oxide and the inner layer is enriched with chromium. However, for the inner layer, enriched manganese has been observed whereas the enrichment of silicon content is not as obvious as that in UP-FM-4. The outer layer mainly consists of magnetite and the inner layer mainly consists of iron-chromium spinel. [3]

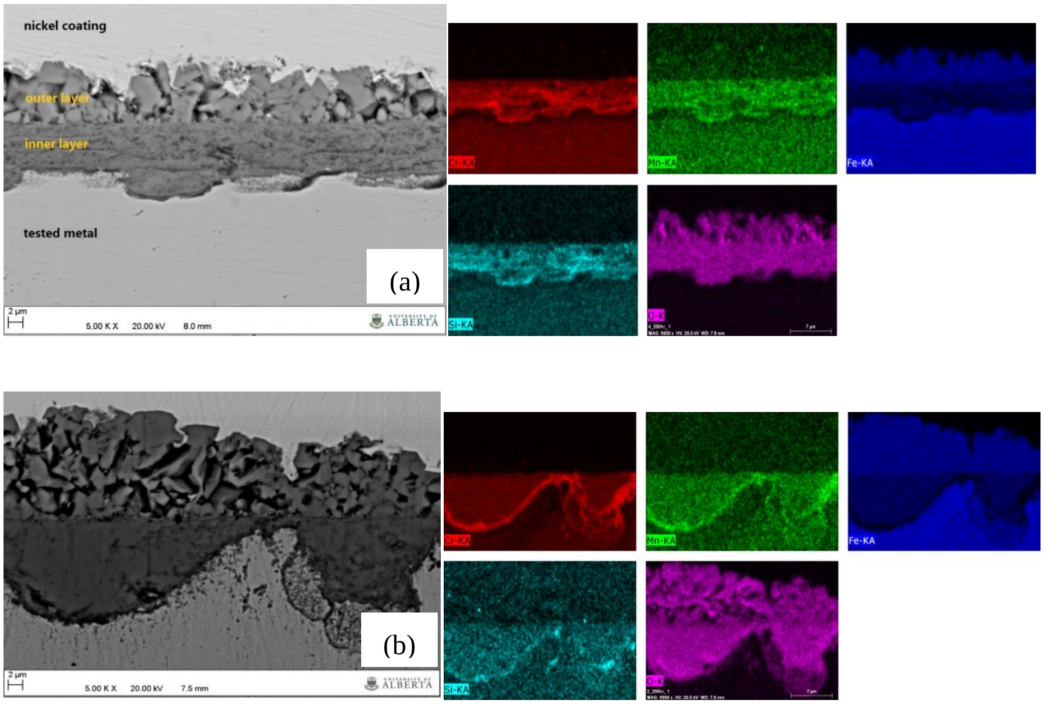

Figure 4.5 *- The cross-section SEM image and EDS mapping of (a) UP-FM-4 and (b) UP-FM-5 after 1000 hour exposure in 500 ℃, 25MPa supercritical water with 8ppm dissolved oxygen. (red: Cr, green: Mn, blue: Fe, cyan: Si, purple: O)*

4.4 Discussion

4.4.1 Effect of minor alloy element on corrosion in supercritical water

The effect of alloy element on corrosion behavior of ferritic-martensitic steels has been investigated by many researchers, but most of their studies only focus on the effect of the chromium element. Little investigations have been taken to study the effect of other alloy elements on corrosion behavior of ferritic-martensitic steels in SCW. According to some papers on the corrosion behavior of ferritic-martensitic steels [27], some minor elements like silicon and manganese have considerable effect on corrosion behavior.

In this study, Samples UP-FM-1, UP-FM-2, and UP-FM-5 were employed to examine the influence of Mn content on corrosion in SCW, since all the alloy elements are very similar except the manganese content that changes from 0.6 wt.% to 1.8 wt.%.

Table 4.3 *- samples used to investigate the effect of manganese element*

Name	Size	Surface treatment	Alloy element (wt%)			
			Cr	Si	**Mn**	Fe
UP-FM-1	20mm×5mm ×2mm	Polished to #1200 grit	11.1	0.7	**0.6**	Balance
UP-FM-2			11.2	0.7	**1.1**	Balance
UP-FM-5			11.7	0.6	**1.8**	Balance

Figure 4.6 shows the weight change data of these samples exposed to 500℃, 25MPa supercritical water with 8 ppm dissolved oxygen. For all samples tested in the low dissolved oxygen supercritical water, a trend has been found that the more weight gain was measured for the sample with higher Mn content. The weight gain of UP-FM-5(1.8% Mn) is about 15% larger than that of UP-FM-1 (0.6 Mn).

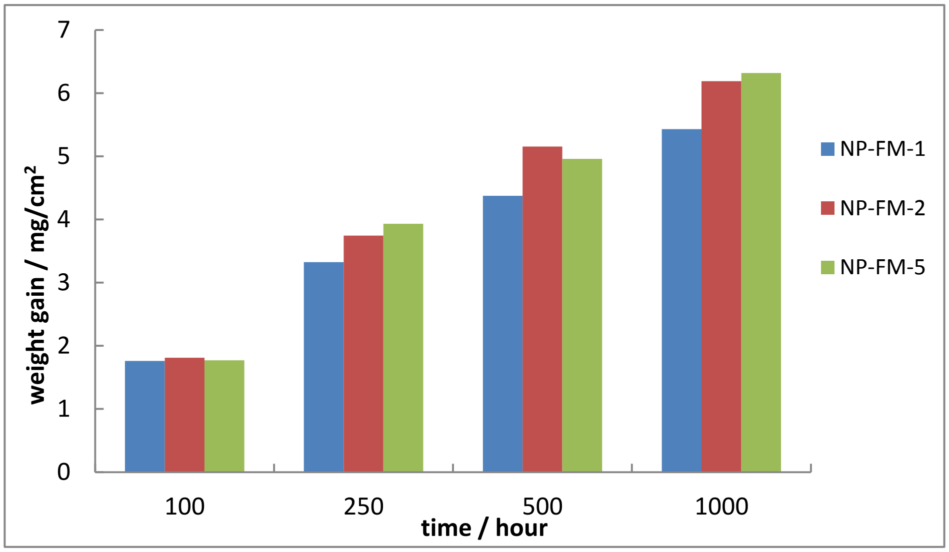

Figure 4.6 - *Weight change as a function of exposure time in 500 ℃, 25MPa supercritical water with 8 ppm dissolved oxygen.*

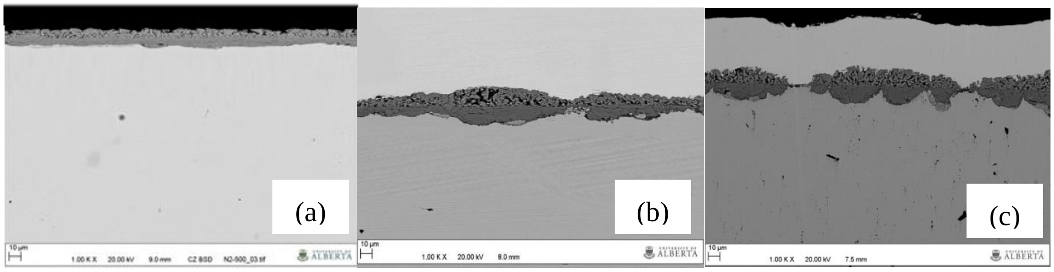

Figure 4.7 - *cross-section SEM images of (a) UP-FM-1, (b) UP-FM-2 and (c) UP-FM-5 after 1000 hour exposure in supercritical water with 8 ppm dissolved oxygen.*

The oxide scales for the samples with different Mn content were shown in Figure 4.7. When the Mn content is at 0.6 wt. %, , a continuous bi-layer oxide scale was formed as shown in Figure 4.7(a). The thickness is about 15~20μm. When the Mn content increased to 1.1 wt. %, the oxide became less uniform in thickness. The thickness of the oxide scale varied from 20 to 30μm. When the Mn content increased to 1.8wt. %, the oxide scale became discontinues and thicker oxide scales about 40μm were formed.

Samples UP-FM-3, UP-FM-4, and UP-FM-5 can imply the effect of silicon on corrosion behavior in supercritical water, since the silicon contents are different while other alloy elements are very similar, as listed in Table 4.4.

Table 4.4 *- Samples used to investigate the effect of silicon element.*

Name	Size	Surface treatment	Alloy element (wt%)			
			Cr	**Si**	Mn	Fe
UP-FM-3	20mm×5mm ×2mm	Polished to #1200 grit	11.6	**1.1**	1.8	balance
UP-FM-4			11.6	**2.2**	1.7	Balance
UP-FM-5			11.7	**0.6**	1.8	Balance

Figure 4.8 shows the weight change data of these samples exposed in 500℃, 25MPa supercritical water with 8 ppm dissolved oxygen. It can be seen that less weight gain was observed for the samples containing more Si. Sample NP-FM-5, which has the smallest Si content of 0.6 wt. %, shows the largest weight gain, whereas the NP-FM-4 with the largest Si content of 2.2wt. % shows the smallest weight gain. After 500 hour exposure, the weight gain measured for Sample NP-FM-5 is about 15% higher than that of NP-FM-4.

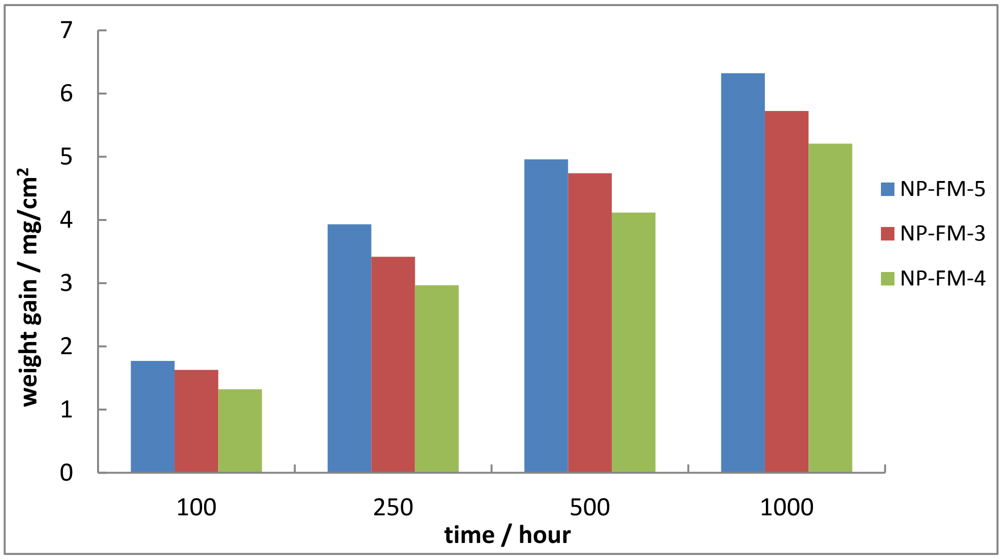

Figure 4.8 - *Weight change as a function of exposure time in 500 ℃, 25MPa supercritical water with 8 ppm dissolved oxygen.*

Figure 4.9 shows the effect of Si content on the oxide scales formed. It can be seen that the oxide scale changed from discontinues to continues layer when Si content increased from 0.6% to 2.2%. The oxide thickness also decreased from about 35 μm on UP-FM-5 to about 25μm on UP-FM-4. According to EDS and XRD results, all these oxide scales are dual-layer structure with the outer layer consisting of magnetite and the inner layer containing chromium-iron oxide.

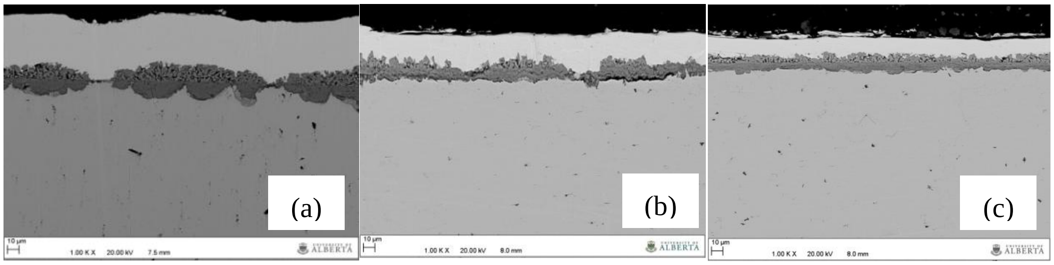

Figure 4.9 *- cross-section SEM images of (a) UP-FM-5, (b) UP-FM-3 and (c) UP-FM-4 after 1000 hour exposure in supercritical water with 8 ppm dissolved oxygen.*

As shown in Figure 4.5, Sample UP-FM-5, which has a Si content of 0.6 wt. %, exhibited an inner oxide layer with the uniform distribution of Si and Cr. However, clear enrichment of Si, Cr and O can be found at the oxide-alloy interface for the Sample UP-FM-4 which has 2.2 wt.% Si. The enrichment of Mn content is not as much as that found in UP-FM-5. When Si content in the alloy increased from 0.6% to 2.2%, enrichment of Si has been found in the inner oxide layer. According to the study by M. Schütze etc, the diffusion of chromium in ferritic-martensitic steels will be facilitated by silicon [27]. So that with higher content of Si were present, the diffusion of Cr could be promoted in UP-FM-4. The faster diffusion of Cr lead to the quick formation of a continuous inner chromium-iron oxide layer as observed for Sample UP-FM-4. This continues chromium-iron oxide layer could act as a diffusion barrier to suppress the transportation of iron (outward) and oxygen (inward). Therefore, a thinner oxide scale and less weight gain were observed for Sample UP-FM-4.

Therefore, both the Si and Mn contents affect the corrosion behavior of ferritic-martensitic steels in supercritical water. The corrosion resistance increased when Si element content increased from 0.6% to 2.2%. On the other hand, the corrosion resistance decreased with increasing the Mn content from 0.6% to 1.8%. The test results indicated that Sample UP-FM-4 with the Si and Mn content of 2.2 wt. % and 1.7 wt. % exhibited the highest corrosion resistance against corrosion in SCW.

4.4.2 Mechanisms of corrosion of Ferritical-Martensitic steels in Supercritical Water Environments

The oxidation mechanism for the corrosion of ferritic-martensitic steels is very complex and governed by the outward migration of iron and the inward diffusion of oxygen. While it is difficult to precisely quantify the oxide layer growth, the outer layer and the inner layer seem to grow at the same time. In the beginning, the oxygen adsorbs on the metal surface forming the iron oxide (outer layer) and creating iron vacancies near the metal surface. The iron from within the grain begins to migrate outwards, drawn by the presence of iron vacancies; thereby enriching the grain it has left in chromium and other minor alloy elements, such as Si and Mn. This process starts to form the outer layer in association with the outwards diffusion of iron. Since the outer layer grows outward from the metal surface, it is not constrained, the Fe_3O_4 grains formed loosely with lots of pores and flaws. At the same time, the oxygen penetrates outer layer through these pores and flaws reaching the metal surface where chromium and other minor elements enriched. It begins to oxidize this layer creating chromium-rich oxide scale (inner layer). Once both layers have formed, the overall oxide layer growth occurs at two interfaces: the outer layer-SCW interface and the inner-metal interface. The outer layer grows by adsorption of oxygen on the surface creating iron vacancies, which migrate inwards along with electron holes, forcing the iron outwards[67]. The oxygen penetrates through the outer layer and oxidizes the layer lack of iron forming the inner layer. Even though this layer attacked by oxygen is enriched with chromium, due to the total content of chromium and diffusion speed of chromium is limited, there is no enough chromium supply to form Cr_2O_3 which exhibits good corrosion resistance. The oxide within inner layer is likely to be $FeCr_2O_4$ which does not have good corrosion resistance.

This enrichment of Si and Mn in the inner oxide layer indicated by the EDS mapping results might have two effects on the corrosion behaviour. Decreasing the Si content or increasing the Mn content might increase the minimum oxygen potential necessary for inner oxide layer formation. Also the Si element might accelerate the diffusion speed of chromium and further increase the corrosion resistance, while the Mn element might slow down the diffusion speed of chromium and further decrease the corrosion resistance.

4.5 Conclusions and future work

In the present study, the corrosion behavior of five kinds of designed ferritic-martensitic steels in supercritical water has been investigated. The effect of alloy elements on the corrosion behavior was discussed. The following conclusions have been drawn from this study.

- The oxides formed on the surfaces of F-M steels exhibited dual-layer structure. The outer layer is predominately magnetite and the inner layer consists of iron-chromium oxide.
- All the samples showed weight gains after supercritical water exposure. The kinetics of oxidation in supercritical water followed the parabolic growth model..
- The oxidation rate is correlative with the alloy composition. The minor alloy element Si and Mn have opposite effects on the corrosion of ferritic-martensitic steels. With increasing Si content, improvement of corrosion resistance has been observed. Less weight gains and thinner, more protective oxide layer were observed for F-M steel containing high Si

content. On the contrary, the weight gains increased and the oxide layers became thicker and less continues when Mn content increased.

Within the scope of study, a few recommendations on the basis of current contribution in this study are:

- Do the supercritical water exposure in more advanced facility which can remain the dissolved oxygen at a constant level and keep flowing, such as supercritical water loop.
- Designed more ferritic-martensitic steels with wider range of Si and Mn content in order to figure out the whole picture of effect of minor alloy element on corrosion in supercritical water.

Chapter 5

Effect of Surface Peening on the Corrosion of Ferritic-Martensitic Stainless Steel in Supercritical Water Environments

5.1 Introduction

Ultrasonic peening, which was one of the effective methods to improve fatigue performance of alloy, has attracted more and more attention for another aspect of application: corrosion control. It has been proved that ultrasonic peening can improve the corrosion resistance in ambient water environment [115]. However, very limited data about the effect of ultrasonic peening on corrosion in supercritical water can be found. This chapter presents the study of the effect of ultrasonic peeing on corrosion of ferritic-martensitic steels in supercritical water. Five kinds of ferritic-martensitic steels with different alloy composition have been investigated. The micro-hardness, oxidation kinetics and oxide scale characterization have been analyzed. The corrosion mechanism and effect of surface peening on corrosion in supercritical water have been discussed.

5.2 Experimental

Table 5.1 gives the information of the specimens used in this study. The preparation is described in chapter 3.

***Table 5.1** – specimens' characterization*

Name	Size	Surface treatment	Alloy element (wt%)			
			Cr	Si	Mn	Fe
P-FM-1	20mm×5mm ×2mm	Ultrasonic peened surface	11.1	0.7	0.6	Balance
P-FM-2			11.2	0.7	1.1	Balance
P-FM-3			11.6	1.1	1.8	Balance
P-FM-4			11.6	2.2	1.7	Balance
P-FM-5			11.7	0.6	1.8	Balance

Supercritical water exposure tests were conducted in static capsule reactors at 500 ℃, 25MPa with 8ppm dissolved oxygen. Exposure time ranges from 100 hours to 1000 hours. After supercritical water exposure, weight changes of specimens were recorded after each test. SEM, EDS and XRD tests have been conducted to characterize the oxide scales formed.

5.3 Results

5.3.1 Micro-hardness characterization

Samples after ultrasonic peening usually form a layer with severe plastic deformation. In order to quantify the depth of this layer, micro-hardness tests were conducted on the peened surface of each sample. The hardness at 25μm, 50μm, 100μm, 150μm and 200μm depth from the surface has been tested. At least 3 points have been tested at each depth. Figure 5.1 and Figure 5.2 showed the micro-hardness tested on ultrasonic peened samples and polished samples.

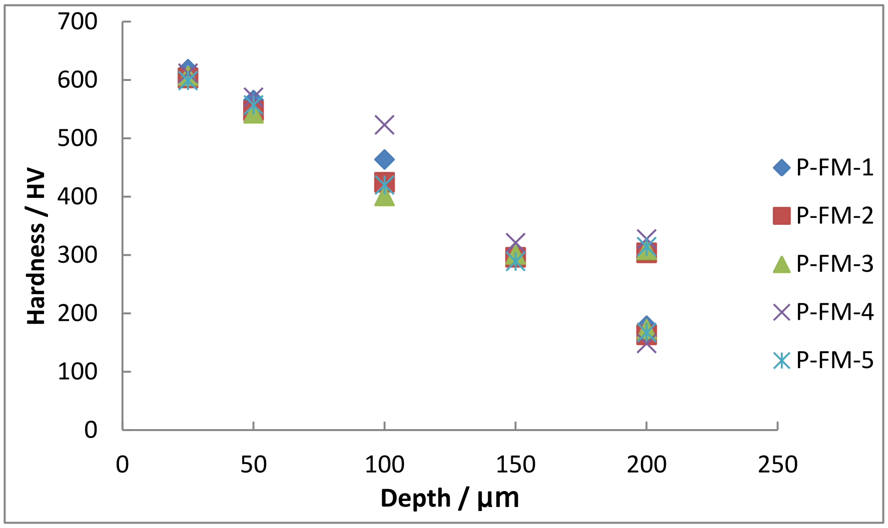

Figure 5.1 *- Micro-hardness test results of ultrasonic peened samples.*

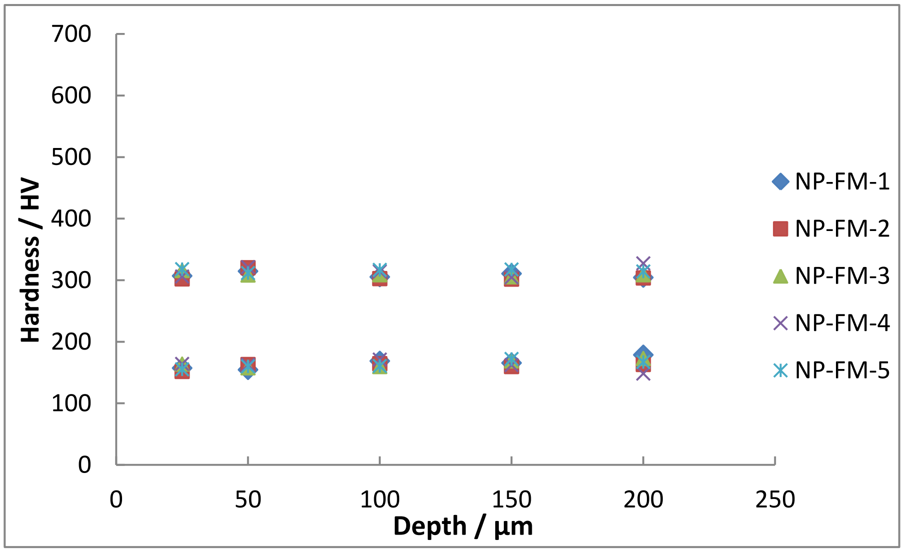

Figure 5.2 *- Micro-hardness test results of polished samples.*

As the materials used in tests are ferritic-martensitic steels, from Figure 5.2, it was obvious that there were two phases with different hardness in the polished samples. The hardness of ferrite phase in these materials is about 170 HV, and the hardness of martensite phase in these materials is about 310 HV. The hardness of ferrite and martensite had almost no change from 25μm deep to 200μm deep from the surface.

However, things were quite different for the ultrasonic peened samples. From Figure 5.1, it was hard to figure out two different phases because there was no significant difference in hardness. The hardness of the surface layer (with depth<100μm) was significantly higher than the polished samples and the value of hardness decreased with increasing the depth. All the five kinds of F-M steels had the same trend. This hardness test results indicated that there was a hardened layer with a depth around 100μm formed induced by the severe plastic deformation after ultrasonic peening treatment.

5.3.2 Oxidation kinetics

Figure 5.3 showed the weight changes of ultrasonic peened ferritic-martensitic steels as a function of exposure time in supercritical water at 500 ℃, 25MPa with 8ppm dissolved oxygen.

For all the peened specimens, weight gains increased with increasing the exposure time. All the peened samples showed much smaller weight gain than the polished samples in all the tested time range as shown in Figure 5.3. The weight gain differences between polished samples and peened samples became more distinct after 500 hour exposure. After 1000 hour exposure, the weight gains of polished samples were about 2 times of the peened ones. For all the ultrasonic peened samples, after 1000 hour exposure, P-FM-1 had smallest weight gain about 2.806 mg/cm^2 and P-FM-5 got largest weight gain about 3.862 mg/cm^2.

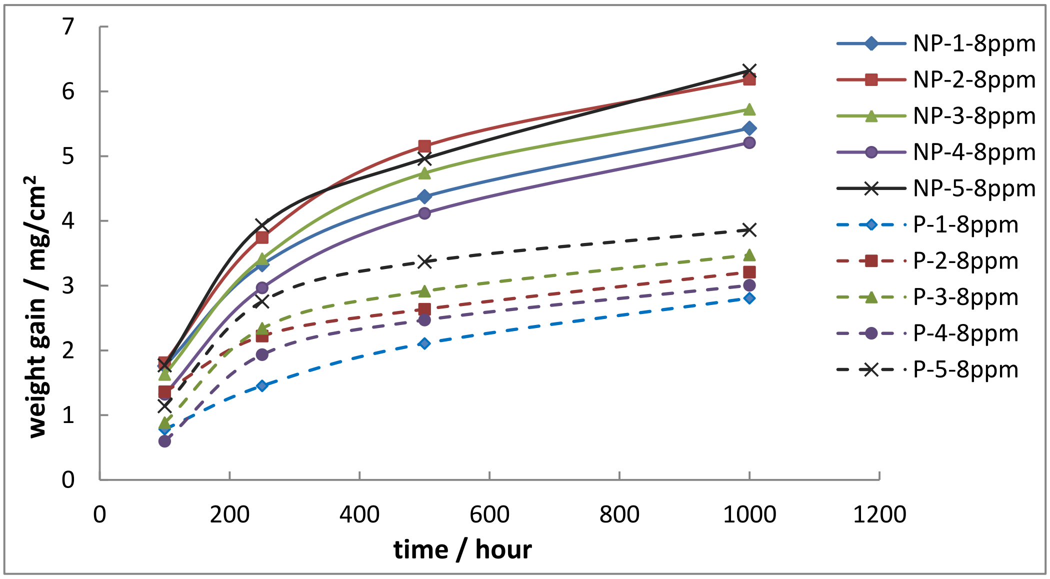

Figure 5.3 *– Comparison of weight gains of polished samples and peened samples.*

Just like what has been found on the polished samples, the oxidation of ultrasonic peened ferritic-martensitic steels also followed the parabolic law. The parabolic constants were derived according to $(\frac{\Delta M}{S})^2 = A + k_p t$, which are listed in Table 5.2. For the ultrasonic peened samples, P-FM-5 presented the largest rate constant which was 0.0094 and P-FM-4 presented lowest oxidation rate as the constant was 0.0069. It can be seen that the unpeened samples have the larger parabolic rate constants than that of peened samples. For the unpeened samples, the largest parabolic rate constant which is 0.0326 came from UP-FM-5 and the smallest rate constant is 0.0238, from UP-FM-4.The parabolic rate constants of polished samples were about 3 times of the constants of the peened ones.

***Table 5.2** - The parabolic rate constants. (Calculation is in Appendix 1)*

Name	Surface treatment	Parabolic rate constant ($mg^2cm^{-2}h^{-2}$)
		8ppm dissolved oxygen
P-FM-1	Ultrasonic peened surface	0.0076
P-FM-2		0.0071
P-FM-3		0.0086
P-FM-4		0.0069
P-FM-5		0.0094
UP-FM-1	Polished surface (up to 1200# grit)	0.0240
UP-FM-2		0.0311
UP-FM-3		0.0270
UP-FM-4		0.0238
UP-FM-5		0.0324

5.3.3 Characterization of oxide scales

Figure 5.4 shows the comparison of surface morphology images from polished specimen (a) UP-FM-4, (b) UP-FM-5 and ultrasonic peened specimen (c) P-FM-4 (d) P-FM-5 after 1000 hours exposure in supercritical water at 500℃ and 25MPa. It can be seen that the peened surfaces were uniformly covered by the oxide particles formed. It is obvious that the oxide particles formed on peened surfaces are much smaller than that formed on polished surfaces. The size of the oxide crystal formed on polished surface is about 7~8 μm whereas the oxide crystal size on peened surface is only about 1 μm. According to the XRD analysis, all the surface oxides were determined to be magnetite.

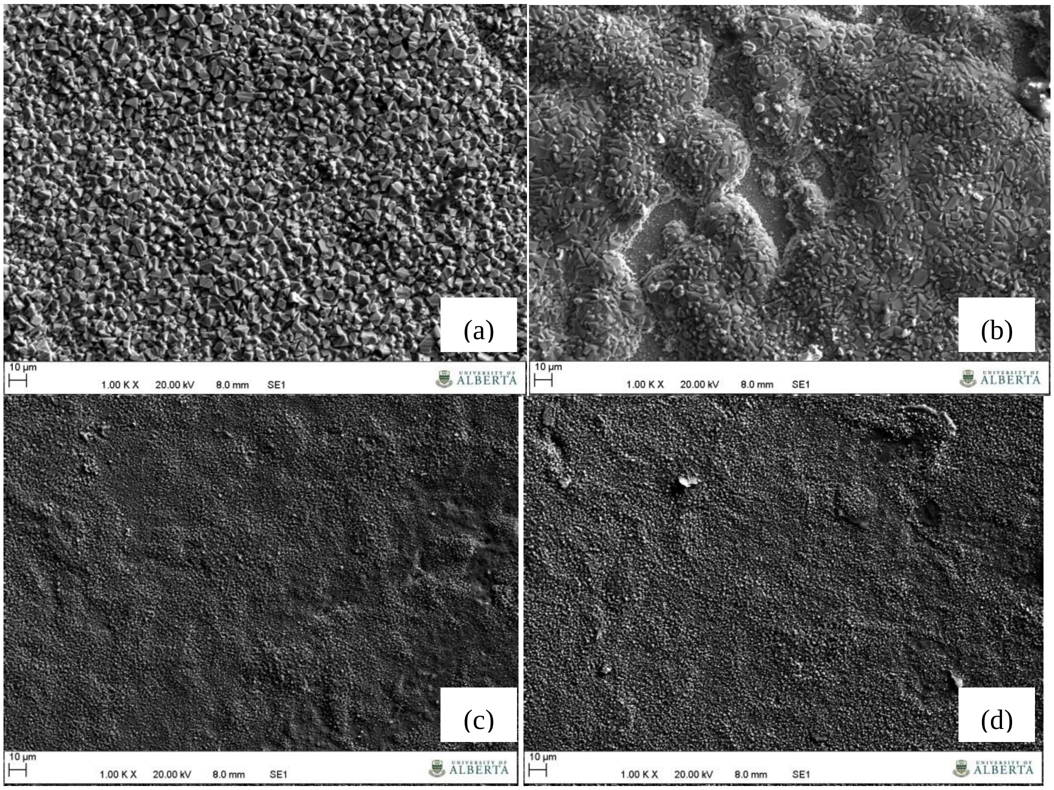

Figure 5.4 *– Surface morphologies comparison: polished specimen (a) UP-FM-4, (b) UP-FM-5 and ultrasonic peened specimen (c) P-FM-4 (d) P-FM-5 after 1000 housr exposure in supercritical water at 500 ℃ and 25MPa.*

Figure 5.5 shows the comparison of Cross-section SEM images and local EDS mappings of polished and peened samples after 1000 hours exposure in supercritical water with 8 ppm dissolved oxygen. According to the SEM images, continuous oxide layer has been observed on all the peened samples. For sample UP-FM-5 and P-FM-5, which have the same chemical composition (11.7% Cr, 0.6% Si and 1.8% Mn), different oxide structures have been observed. Thinner and continues oxide layer has been found on the peened P-FM-5 while thicker and discontinues layer formed on the polished UP-FM-5. Moreover, the outer oxide layer on the peened surface is more compact than the outer layer formed on the polished surface. Similar phenomenon has and been found on Samples UP-FM-2 , P-FM-2, UP-FM-3 and P-FM-3. For sample UP-FM-4 and P-FM-4, which have the same chemical composition (11.6% Cr, 2.2% Si and 1.7% Mn), the oxide layers on both polished and peened samples are all continues. But the oxide layer formed on peened sample is only about 10μm thick, which is much thinner than that (30μm) formed on polished samples. The oxidation behavior of UP-FM-1 and P-FM-1 pair is quite similar to UP-FM-4 and P-FM-4 pair. The oxide thickness of the peened samples is about 1/3 to half of the thickness of oxide layer formed on the polished samples. The thickness of oxide layer coincides with the weight change data. Based on the EDS mappings, it is obvious that all the oxides have dual layer structure. The outer layer is predominately magnetite while the inner layer consists of iron-chromium oxide. However, a big difference of chromium enrichment in the inner layer has been observed between peened and polished samples. For the polished samples, less enrichment of chromium were observed than that of the peened samples. Furthermore, the distribution of the enriched chromium in inner layer is more homogeneous in the peened samples than that in polished samples indicating that a more homogeneous chromium-iron oxide layer has been formed on the peened samples.

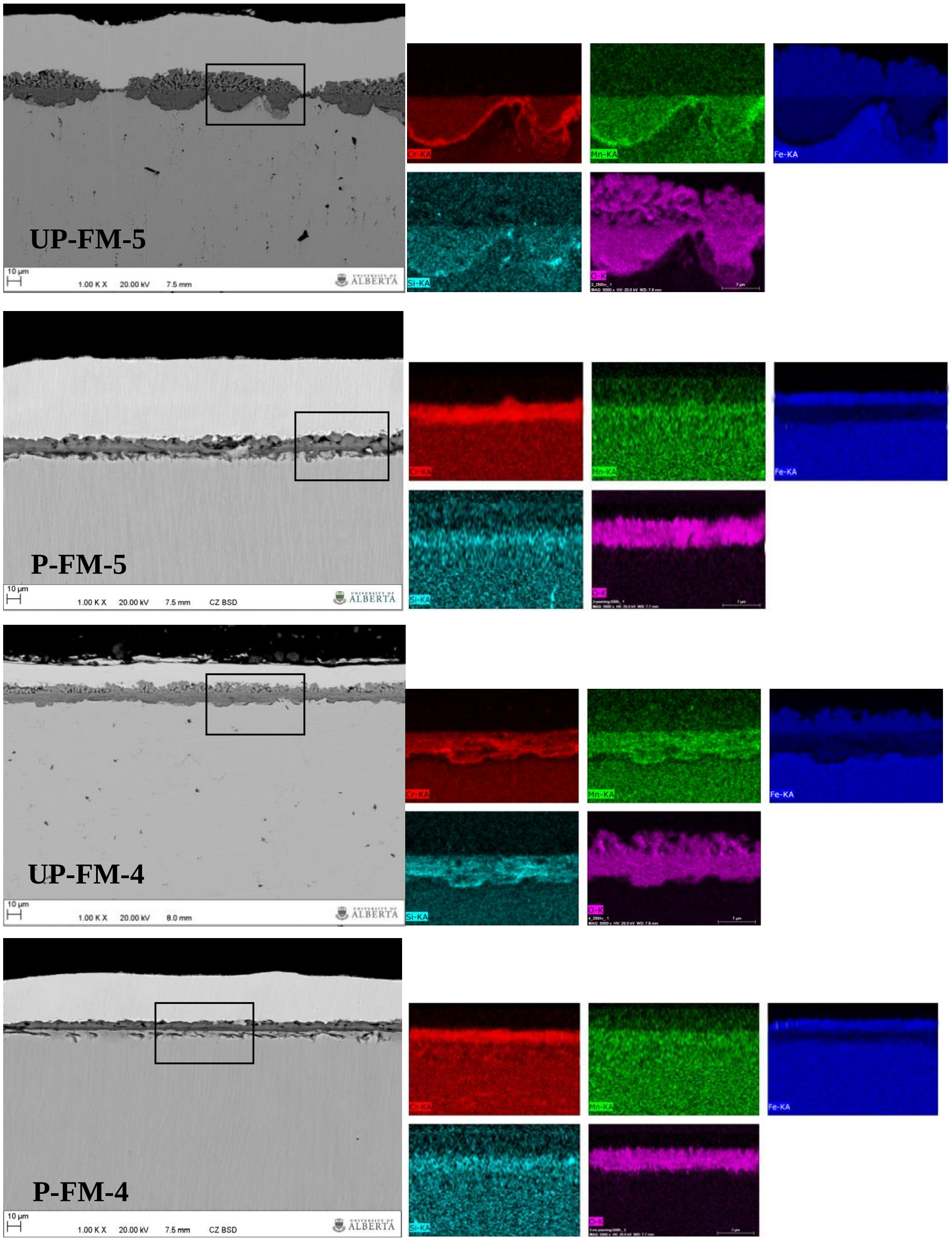

Figure 5.5- *Cross-section SEM images and local EDS mappings of polished and peened samples after 1000 hours exposure in supercritical water with 8 ppm dissolved oxygen. (red: Cr, green: Mn, blue: Fe, cyan: Si, purple: O).*

5.4 Discussion

5.4.1 Role of shot peening in oxidation in supercritical water

To demonstrate the effect of ultrasonic peening in terms of parabolic rate constant, a parameter, corrosion resistance improvement by ultrasonic peening (CRIUP) is defined as below:

$$\text{CRIUP} = \frac{PRC_{Polished} - PRC_{Peened}}{PRC_{Polished}} \times 100\%$$

where the $PRC_{Polished}$ and PRC_{Peened} are the parabolic rate constant data of polished and peened samples respectively. By definition, the larger the CRIUP, the more corrosion improvement can be achieved by ultrasonic peening. CRIUP percentages of FM-1 to FM-5 are shown in Figure 5.6. From the CRIUP data, distinct corrosion improvement has been achieved by ultrasonic peening in supercritical water. For all the steels tested, the best case has been found in FM-2 (11.2% Cr, 0.7 % Si, and 1.1% Mn), for which the CRIUP is 77.17%, and the worst case has been found in FM-3 (11.6% Cr, 1.1% Si and 1.8% Mn), for which the CRIUP is 68.15%. According to the research by X. Ren etc. the corrosion resistance improvement of ferritic-martensitic steels achieved by shot peening is proportional to the chromium content in bulk material [86]. As the chromium contents are very similar in all the materials used in this study, relationship between the alloy composition and the corrosion resistance improvement achieved by ultrasonic peening is not straight forward. The Si and Mn content may have some effects on the ultrasonic peening effect, but more data are needed to identify their effects.

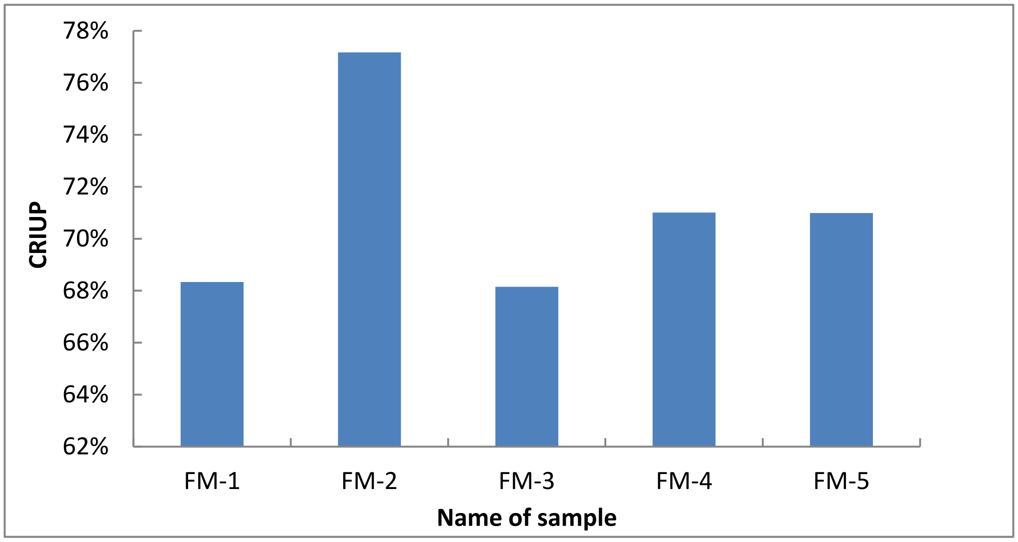

Figure 5.6 *- CRIUP percentages of FM-1 to FM-5*

5.4.2 Mechanism of corrosion of ferritic-martensitic steels with ultrasonic peening treatment in supercritical water

The oxidation mechanism for the corrosion of ferritic-martensitic steels with ultrasonic peening treatment in supercritical water is very similar with the mechanism of the one without peening and still governed by the outward migration of iron and the inward diffusion of oxygen. However, the severe plastic deformation layer induced by ultrasonic peening plays an important role in the corrosion process. Amount of micro-cracks and dislocations have been generated within this plastic deformation layer during ultrasonic peening. All these micro-cracks and dislocations are short-circuit paths for ion diffusion, especially the diffusion of Cr element. Therefore, the diffusion of Cr during supercritical water exposure could be accelerated, leading to more supplement of Cr when forming inner oxide layer. Under this condition, Cr_2O_3, instead of $FeCr_2O_4$, begins to present in the inner oxide layer. Cr_2O_3 acted as barrier for both the inward penetration of oxygen and the outward diffusion of metal ions. Therefore, the oxidation rate was evidently decreased.

5.5 Conclusions and future work

In the present study, the corrosion behavior of five kinds of designed ferritic-martensitic steels with ultrasonic peening in supercritical water has been investigated. Conclusions have been drawn in the following aspects.

- After ultrasonic peening, a severe plastic deformation layer with a thickness of 80~100 µm formed on the peened metal surface.
- Dual-layer oxide scales formed after supercritical water exposure. The outer layer is predominately magnetite and the inner layer is iron-chromium oxides. Comparing to the discontinuous oxide scales found on the polished specimens, the oxide scales formed on all the peened specimens were continuous. For samples with same alloy composition, the

polished sample formed oxide scales about 3 times thicker than that of the peened sample.

- For samples with same alloy composition, the peened sample showed about 50% smaller weight gains than the polished sample. And the parabolic rate constant of peened sample was about 1/3 of that of polished sample.
- Overall, ultrasonic peening improved the corrosion behavior of ferritic-martensitic steel in supercritical water environment.

Within the scope of study, a few recommendations on the basis of current contribution in this study are:

- Exposure in supercritical water for longer time is recommended to prove the positive effect of ultrasonic peening on corrosion of ferritic-martensitic steels.
- Exposure test is recommended to be conducted in supercritical loop instead of capsule sample in order to get an environment closer to the industry application.

Chapter 6

Effect of Dissolved Oxygen on the Corrosion of Ferritic-Martensitic Stainless Steels in Supercritical Water

6.1 Introduction

As one of the key parameters of supercritical water, dissolved oxygen concentration plays an important role in corrosion in supercritical water. As the corrosion in supercritical water is not electrochemical process but only chemical oxidation process, the corrosion is determined by the supply of oxygen to some extent [3]. This chapter presents the study of the effect of dissolved oxygen on corrosion of ferritic-martensitic steels in supercritical water. Five kinds of ferritic-martensitic steels with different alloy composition have been investigated. The oxidation kinetics and oxide scales formed have been studied. The corrosion mechanism and effect of dissolved oxygen on corrosion in supercritical water have been discussed.

6.2 Experimental

Table 6.1 shows the specimens used for this study. The preparation is described in chapter 3. Supercritical water exposure tests have been conducted in capsule autoclaves at 500 ℃, 25MPa with two oxygen concentrations. The SCW environment with the high oxygen concentration was obtained by adding H_2O_2 into the deionized water to get 5vol% H_2O_2 solution, and then sealed in capsules, in order to compare the corrosion behavior in high dissolved oxygen. The oxygen content inside the capsules can be increased to 22000 ppm. For the SCW with low dissolved oxygen, the de-ionized water with 8 ppm oxygen concentration was used as the test liquid. Exposure Time lasted from 100 hours to 1000 hours. After supercritical water exposure, weight changes of specimens have been measured in order to investigate the oxidation kinetics. SEM, EDS and XRD have been applied to characterize the surface and cross-section morphologies and compositions of oxide scales.

Table 6.1 *- The main parameters of samples used for high dissolved oxygen supercritical water exposure.*

Name	Size	Surface treatment	Alloy element (wt%)			
			Cr	Si	Mn	Fe
P-FM-1	20mm×5mm ×2mm	Ultrasonic peened surface	11.1	0.7	0.6	Balance
P-FM-2			11.2	0.7	1.1	Balance
P-FM-3			11.6	1.1	1.8	Balance
P-FM-4			11.6	2.2	1.7	Balance
P-FM-5			11.7	0.6	1.8	Balance
UP-FM-1	20mm×5mm ×2mm	Polished surface (up to 1200# grit)	11.1	0.7	0.6	Balance
UP-FM-2			11.2	0.7	1.1	Balance
UP-FM-3			11.6	1.1	1.8	Balance
UP-FM-4			11.6	2.2	1.7	Balance
UP-FM-5			11.7	0.6	1.8	Balance

6.3 Results

6.3.1 Oxidation kinetics

Figure 6.1 shows the comparison of weight change data of samples exposed to supercritical water with different dissolved oxygen concentrations. Increase of weight gain has been found in both peened samples and polished samples when dissolved oxygen concentration increased. After 1000 hour exposure, the weight gains of samples exposed in supercritical water with 5% H_2O_2 were about 2 times higher than that of samples exposed to supercritical water with 8ppm dissolved oxygen. In both low and high dissolved oxygen, the oxidation behaviors of all ferritic-martensitic steels roughly followed the parabolic laws. However, the parabolic rate constant increased when dissolved oxygen concentration increased.

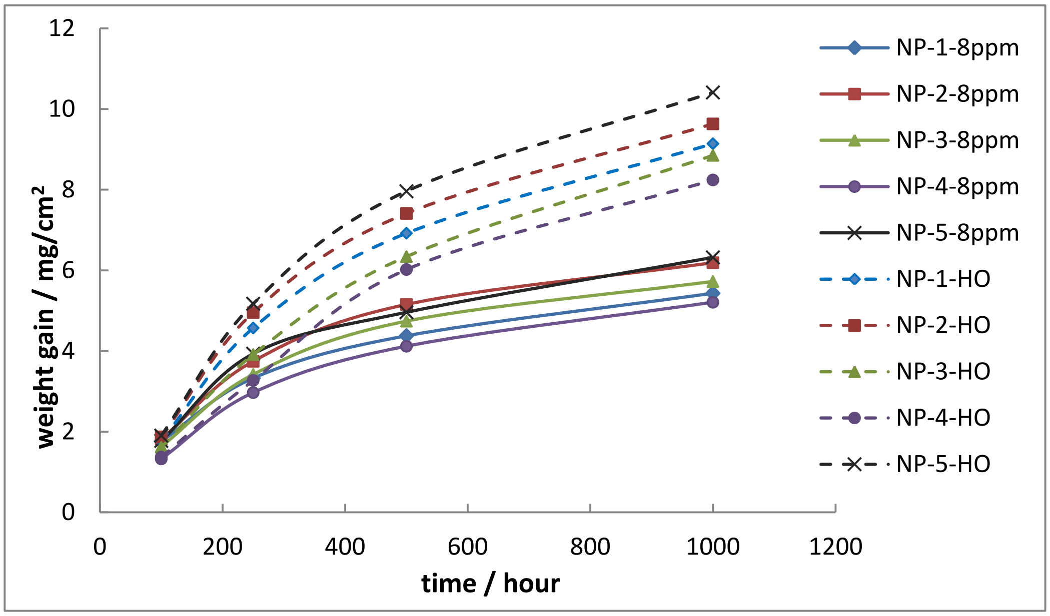

(a)

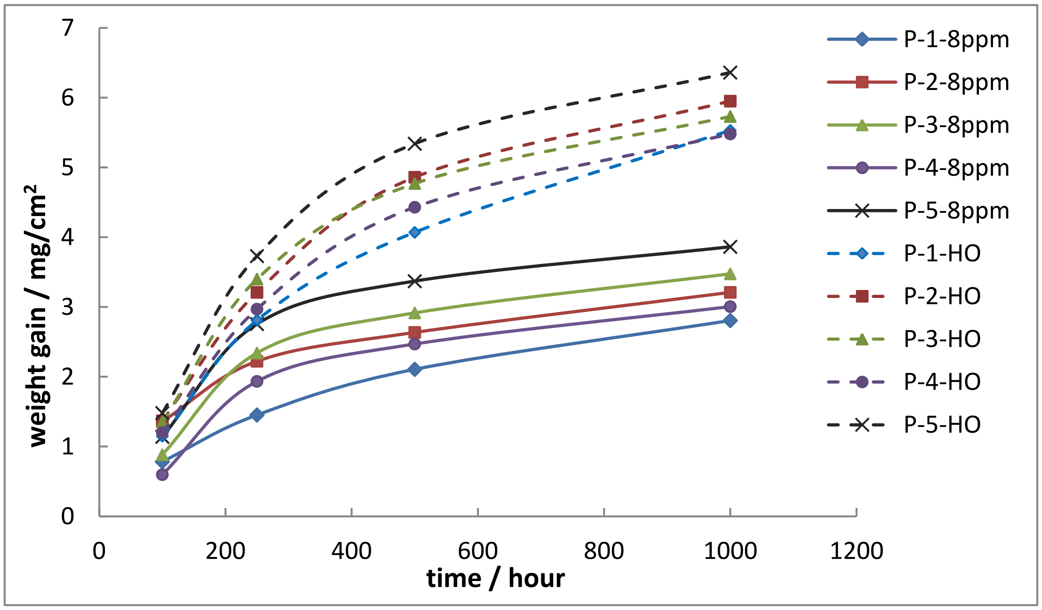

(b)

Figure 6.1 *- Weight change as a function of exposure time in supercritical water with different dissolved oxygen concentration. (a) Unpeened samples, (b) ultrasonic peened samples. (Dashed: weight gain in high dissolved oxygen. Solid: weight gain in low dissolved oxygen.)*

Table 6.2 shows the comparison of parabolic rate constant in supercritical water with different dissolved oxygen concentrations. The oxidation rate is proportional to the parabolic rate constant, so the parabolic rate constant indicates how fast the oxidation could happen.

Table 6.2 *- The parabolic rate constant. (Calculation is in Appendix 1)*

Name	Surface treatment	Parabolic rate constant ($mg^2cm^{-2}h^{-2}$)	
		8ppm dissolved oxygen	5% H_2O_2 added
P-FM-1	Ultrasonic peened surface	0.0076	0.0319
P-FM-2		0.0071	0.0365
P-FM-3		0.0086	0.0330
P-FM-4		0.0069	0.0310
P-FM-5		0.0094	0.0408
UP-FM-1	Polished surface (up to 1200# grit)	0.0240	0.0881
UP-FM-2		0.0311	0.0973
UP-FM-3		0.0270	0.0844
UP-FM-4		0.0238	0.0748
UP-FM-5		0.0324	0.1149

With the SCW environment changed from 8 ppm deionized water to 5% H_2O_2 solution, the parabolic rate constants increased more than threefold for all the tested samples. As the oxidation is roughly controlled by parabolic law, the diffusion of cationic and anionic species through oxide scale is the controlling factor. The increase of parabolic rate constant indicates that the oxidation rate increases with the increase of dissolved oxygen. It means that the dissolved oxygen concentration may accelerate the diffusion of cationic and anionic species through oxide scale. In another aspect, the more oxygen supplied leads to more oxide growth, so that more weight gain was observed.

6.3.2 Characterization of oxide scales

Different oxide scales have been observed in tests with different dissolved oxygen concentration. Figure 6.2 shows the comparison of surface morphologies of specimens exposed to supercritical water with different dissolved oxygen. The oxide formed in lower dissolved oxygen has larger grain size about 7~8μm. The grain size of oxide formed in SCW with high dissolved oxygen is smaller around 1~2μm. According to the XRD analysis as shown in figure 6.3, the surface oxide scales were determined as hematite.

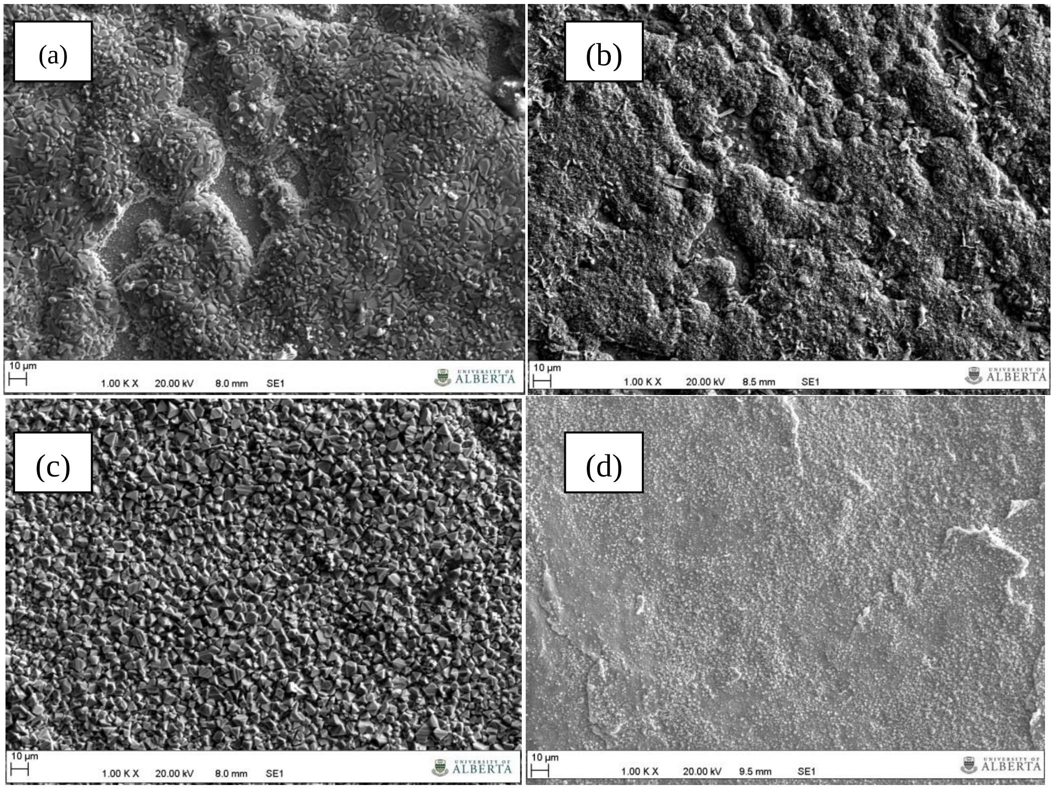

Figure 6.2 *- Surface morphology SEM images: exposure time:1000 hours (a) UP-FM-5 in low dissolved oxygen (b) UP-FM-5 in high dissolved oxygen (c) UP-FM-4 in low dissolved oxygen (d) UP-FM-4 in high dissolved oxygen.*

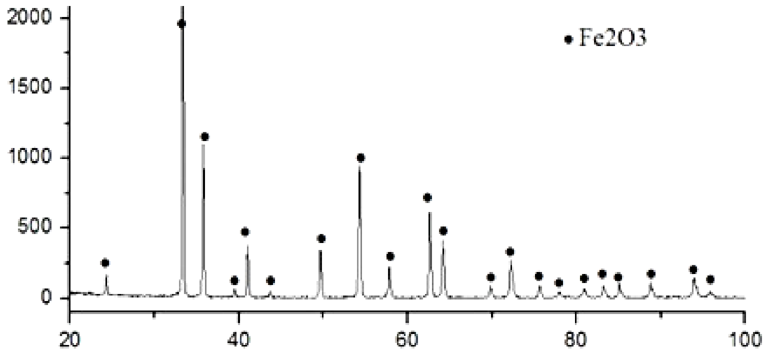

Figure 6.3 *- XRD result of the surface oxide scale formed on UP-FM-5 after 1000 hour exposure in high dissolved oxygen supercritical water*

Figure 6.4 shows the comparison of cross-section of oxide scales formed in supercritical water with different dissolved oxygen concentrations.

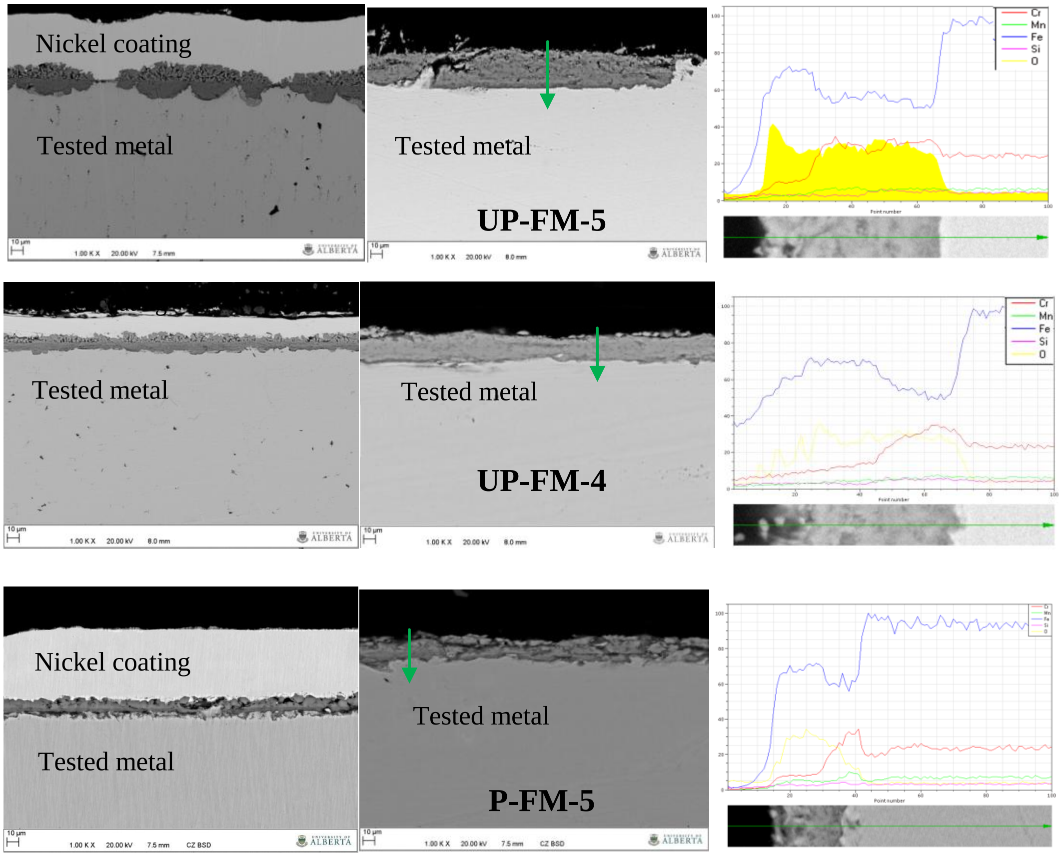

(a) (b) (c)

Figure 6.4 *- Cross-section SEM images of sample UP-FM-5, UP-FM-4 and P-FM-5 after 1000 hour exposure in supercritical water with (a) low dissolved oxygen concentration, (b) high dissolved oxygen concentration and (c) EDS linear scan of oxide scale formed in high dissolved oxygen SCW.*

The oxide formed in supercritical water with the high dissolved oxygen concentration is more continues and more uniform than the oxide formed in supercritical water with the low dissolved oxygen. It is obvious that the oxide thickness increased with increasing the dissolved oxygen. The oxide thickness increased to about 2 times in high oxygen SCW, which is consistent with the weight gain data. The oxide formed in supercritical water with low dissolved oxygen has relatively distinct dual layer structure, whereas the oxide formed in supercritical water with high dissolved oxygen exhibited a single-layer structure. However, according to the EDS linear scanning and XRD data, the oxide in high dissolved oxygen still has a dual layer structure. The outer layers of the samples exposed to low dissolved oxygen are predominately magnetite while the outer layers of samples in high dissolved oxygen consist of hematite. All the inner layers consist of iron-chromium oxide. Although the outer layer and inner layer of oxide formed in high dissolved oxygen have different composition, their structures are very similar in SEM images. The increase of dissolved oxygen concentration makes the outer layer more uniform and more condensed. This is because the more oxygen supplied, the more oxide grew and developed into a continuous and uniform structure.

Because of the test facility used in this study, there are some limitations for studying the effect of dissolved oxygen on corrosion behavior of ferritic-martensitic steels in supercritical water. As all the tests are static tests conducted in capsules, the oxygen concentration might drop with increasing the exposure time. Because of the oxidation consumption, the dissolved oxygen concentration dropped when SCW exposure test began. It means the dissolved oxygen concentration is not constant or stable during the exposure but decreases when time increases.

6.4 Discussion

6.4.1 Effect of alloy element on corrosion in high dissolved oxygen

Figure 6.5 shows the weight change data of these samples exposed in 500℃, 25MPa supercritical water with H_2O_2 added. For tests in high dissolved oxygen supercritical water, the effect of Mn on weight change is similar to the effect found in low dissolved oxygen. However, in the high dissolved oxygen environment, the weight gain of each sample, both the polished and peened, got closer to each other. For polished samples after 1000 hour exposure, the weight gain of UP-FM-5 is nearly 10% larger than that of UP-FM-1. And after 1000 hour exposure, the weight gain of peened sample P-FM-5 is 15% larger than that of P-FM-1. It can be seen that the effect of Mn has been weakened by the high dissolved oxygen.

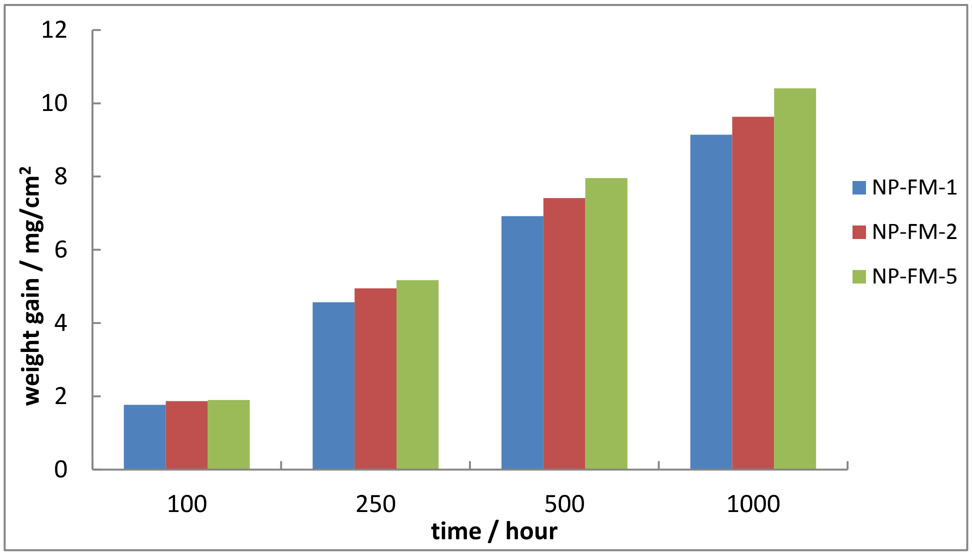

(a)

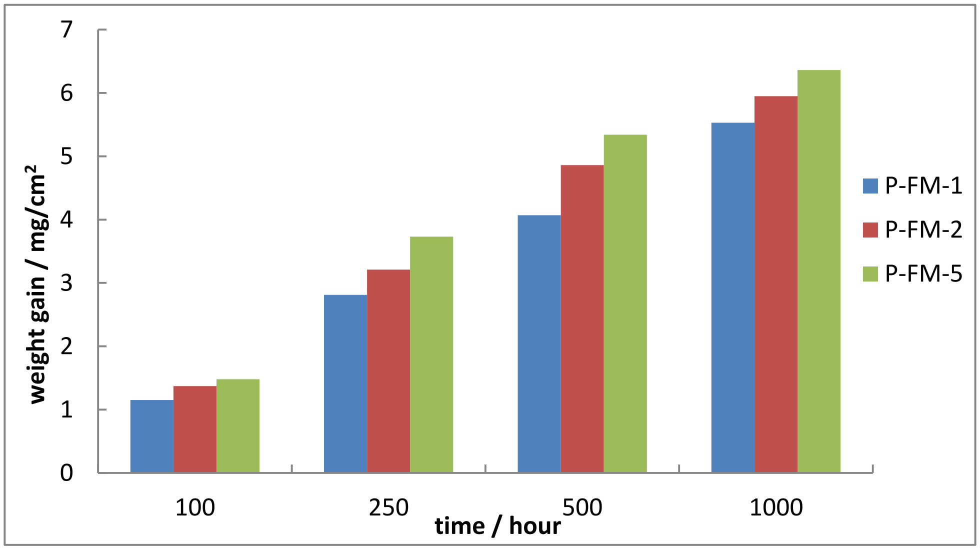

(b)

Figure 6.5 *- Weight change as a function of exposure time in 500 ℃, 25MPa supercritical water with* H_2O_2 *added. (a) polished samples, (b) ultrasonic peened samples.*

Figure 6.6 shows the weight change data of these samples exposed in 500℃, 25MPa supercritical water with H_2O_2 added. The similar trend has been found in high dissolved oxygen tests. The weight gains decreased when Si content increased from 0.6% to 2.2% for both polished and peened samples. However, the Si effect is weaker in high dissolved oxygen supercritical water than in low dissolved oxygen.

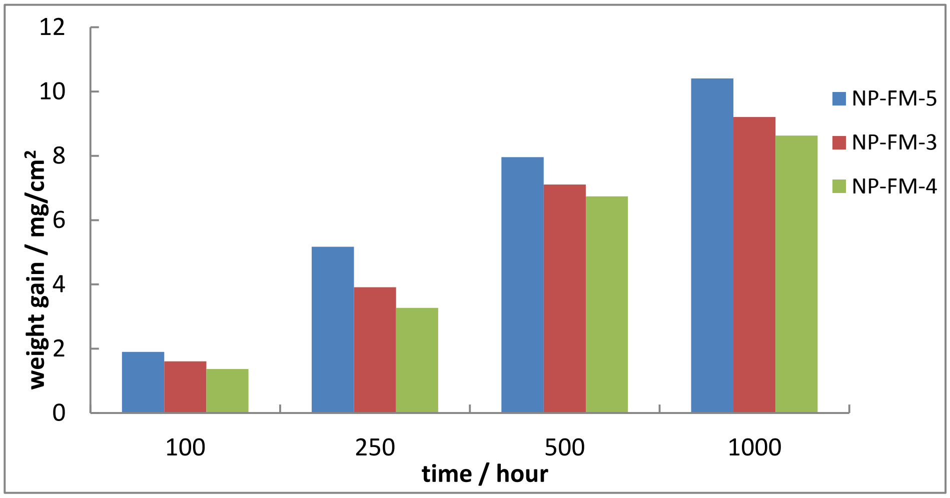

(a)

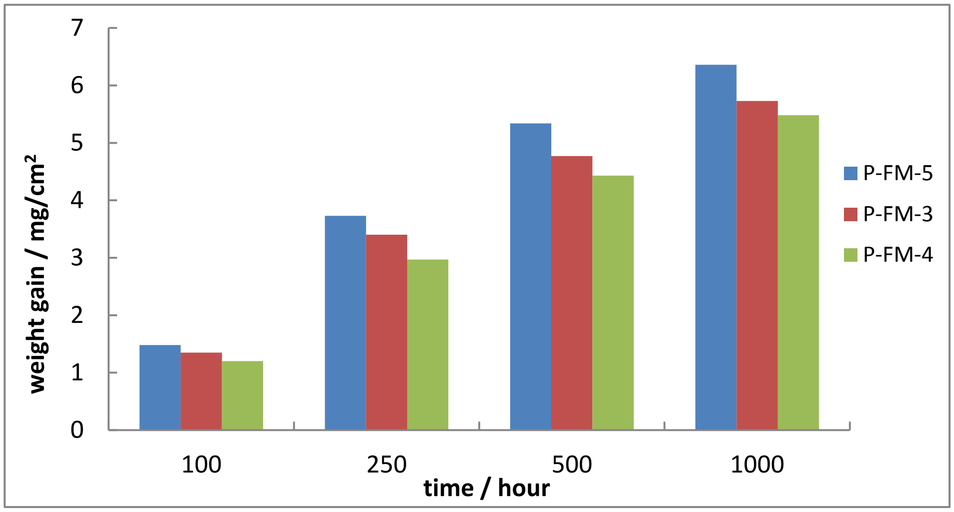

(b)

Figure 6.6 - *Weight change as a function of exposure time in 500 ℃, 25MPa supercritical water with H_2O_2 added. (a) polished samples, (b) ultrasonic peened samples.*

6.4.2 Effect of dissolved oxygen on the formation of the oxide scales

The most distinct effect of dissolved oxygen on the formation of oxide scale is that in high dissolved oxygen supercritical water, hematite has been found within the outer layer. In high dissolved oxygen supercritical water, because of higher partial oxygen pressure, more oxygen can be absorbed and reacted with the iron at the metal-SCW interface, so that Fe_2O_3 formed instead of Fe_3O_4. Moreover, as more oxygen supplied, the more quickly the iron will be consumed, leading to the acceleration of the iron diffusion. Simultaneously, the higher oxygen partial pressure leads to quicker inward oxygen penetration. The accelerated iron diffusion and oxygen penetration lead to fast oxidation rate in supercritical water. According to Renfei Wang's study [132], increasing the dissolved oxygen concentration in SCW can lead to dramatically increasing of the solubility of Cr oxide in SCW. Therefore in high dissolved oxygen SCW environment, chromium oxide became very unstable. As the inner oxide layer consisting of chromium oxide, in high dissolved oxygen SCW, the inner layer became unstable and less efficient for blocking the outward diffusion of iron ion. This may explain why thicker oxide layers and larger weight gains were observed in high dissolved oxygen SCW exposure tests.

6.5 Conclusions and future work

In the present study, the corrosion behavior of five kinds of designed ferritic-martensitic steels in supercritical water with different dissolved oxygen concentration has been investigated. Conclusions have been drawn in the following aspects.

- Dual layer oxide scales formed after supercritical water exposure. The outer layer is predominately hematite and the inner layer is iron-chromium oxide. The outer oxide layer become denser and the distinct line between outer layer and inner layer disappeared after exposure in high dissolved oxygen supercritical water.
- When dissolved oxygen increased from 8ppm to 5% H_2O_2 solution, the weight gains increased significantly and the parabolic rate constants increased about 3 times.
- The effects of alloy element Si and Mn on corrosion in low dissolved oxygen supercritical water (discussed in Chapter 4) have been weakened in high dissolved oxygen environment.

Within the scope of study, a few recommendations on the basis of current contribution in this study are:

- Due to the limitation of capsule sample, it’s hard to keep the dissolved oxygen at constant level. It’s recommended to conduct supercritical water exposure test in facility like supercritical water loop.
- Tests in supercritical water with more variations of dissolved oxygen content are recommended to get the whole picture of the effect of dissolved oxygen on corrosion of ferritic-martensitic steels in supercritical water.

Reference

[1] Ren, X., Sridharan, K., and Allen, T. R., 2010, "Effect of Grain Refinement on Corrosion of Ferritic-Martensitic Steels in Supercritical Water Environment," Materials and Corrosion-Werkstoffe Und Korrosion, **61**(9) pp. 748-755.

[2] Tan, L., Ren, X., Sridharan, K., 2008, "Effect of Shot-Peening on the Oxidation of Alloy 800H Exposed to Supercritical Water and Cyclic Oxidation," Corrosion Science, **50**(7) pp. 2040-2046

[3] Was, G. S., Ampornrat, P., Gupta, G., 2007, "Corrosion and Stress Corrosion Cracking in Supercritical Water," Journal of Nuclear Materials, **371**(1-3) pp. 176-201.

[4] Ampornrat, P., and Was, G. S., 2007, "Oxidation of Ferritic-Martensitic Alloys T91, HCM12A and HT-9 in Supercritical Water," Journal of Nuclear Materials, **371**(1-3) pp. 1-17.

[5] Guo, F. A., Trannoy, N., and Lu, J., 2004, "Microstructural Analysis by Scanning Thermal Microscopy of a Nanocrystalline Fe Surface Induced by Ultrasonic Shot Peening," Superlattices and Microstructures, **35**(3–6) pp. 445-453.

[6] Liu, G., Lu, J., and Lu, K., 2000, "Surface Nanocrystallization of 316L Stainless Steel Induced by Ultrasonic Shot Peening," Materials Science and Engineering: A, **286**(1) pp. 91-95.

[7] Mordyuk, B. N., and Prokopenko, G. I., 2007, "Ultrasonic Impact Peening for the Surface Properties' Management," Journal of Sound and Vibration, **308**(3–5) pp. 855-866.

[8] Bellissent-Funel, M. -., 2001, "Structure of Supercritical Water," Journal of Molecular Liquids, **90**(1–3) pp. 313-322.

[9] Bermejo, M. D., and Cocero, M. J., 2006, "Supercritical Water Oxidation: A Technical Review," AICHE Journal, **52**(11) pp. 3933-3951.

[10] Betova, I., Bojinov, M., Kinnunen, P., 2007, "Surface Film Electrochemistry of Austenitic Stainless Steel and its Main Constituents in Supercritical Water," Journal of Supercritical Fluids, **43**(2) pp. 333-340.

[11] Bischoff, J., Motta, A. T., Eichfeld, C., "Corrosion of Ferritic-Martensitic Steels in Steam and Supercritical Water," Journal of Nuclear Materials, (0) .

[12] Broll, D., Kaul, C., Kramer, A., 1999, "Chemistry in Supercritical Water," Angewandte Chemie-International Edition, **38**(20) pp. 2999-3014.

[13] Brunner, G., 2009, "Near and Supercritical Water. Part II: Oxidative Processes," The Journal of Supercritical Fluids, **47**(3) pp. 382-390.

[14] Brunner, G., 2009, "Near Critical and Supercritical Water. Part I. Hydrolytic and Hydrothermal Processes," The Journal of Supercritical Fluids, **47**(3) pp. 373-381.

[15] Cao, G., Firouzdor, V., Sridharan, K., 2012, "Corrosion of Austenitic Alloys in High Temperature Supercritical Carbon Dioxide," Corrosion Science, **60**(0) pp. 246-255.

[16] Chen, Y., Sridharan, K., and Allen, T., 2006, "Corrosion Behavior of Ferritic-Martensitic Steel T91 in Supercritical Water," Corrosion Science, **48**(9) pp. 2843-2854.

[17] Chen, Y., Sridharan, K., Allen, T. R., 2006, "Microstructural Examination of Oxide Layers Formed on an Oxide Dispersion Strengthened Ferritic Steel Exposed to Supercritical Water," Journal of Nuclear Materials, **359**(1–2) pp. 50-58.

[18] Chen, Y., Sridharan, K., Ukai, S., 2007, "Oxidation of 9Cr Oxide Dispersion Strengthened Steel Exposed in Supercritical Water," Journal of Nuclear Materials, **371**(1-3) pp. 118-128.

[19] Cho, K. T., Yoo, S., Lim, K. M., 2011, "Effect of Si Content on Surface Hardening of Al–Si Alloy by Shot Peening Treatment," Journal of Alloys and Compounds, **509, Supplement 1**(0) pp. S265-S270.

[20] Cochran, H. D., Cummings, P. T., and Karaborni, S., 1992, "Solvation in Supercritical Water," Fluid Phase Equilibria, **71**(1–2) pp. 1-16.

[21] Cook, W. G., and Olive, R. P., 2012, "Pourbaix Diagrams for the iron–water System Extended to High-Subcritical and Low-Supercritical Conditions," Corrosion Science, **55**(0) pp. 326-331.

[22] Dai, K., and Shaw, L., 2007, "Comparison between Shot Peening and Surface Nanocrystallization and Hardening Processes," Materials Science and Engineering: A, **463**(1–2) pp. 46-53.

[23] Daigo, Y., Watanabe, Y., and Sue, K., 2007, "Effect of Chromium Ion from Autoclave Material on Corrosion Behavior of Nickel-Based Alloys in Supercritical Water," Corrosion, **63**(3) pp. 277-284.

[24] Daigo, Y., Watanabe, Y., and Sue, K., 2007, "Corrosion Mitigation in Supercritical Water with Chromium Ion," Corrosion, **63**(12) pp. 1085-1093.

[25] Fujisawa, R., Sakaihara, M., Kurata, Y., 2005, "Corrosion Behaviour of Nickel Base Alloys and 316 Stainless Steel in Supercritical Water Under Alkaline Conditions," Corrosion Engineering Science and Technology, **40**(3) pp. 244-248.

[26] Fulger, M., Ohai, D., Mihalache, M., 2009, "Oxidation Behavior of Incoloy 800 Under Simulated Supercritical Water Conditions," Journal of Nuclear Materials, **385**(2) pp. 288-293.

[27] Gao, X., Wu, X., Zhang, Z., 2007, "Characterization of Oxide Films Grown on 316L Stainless Steel Exposed to H2O2-Containing Supercritical Water," Journal of Supercritical Fluids, **42**(1) pp. 157-163.

[28] Gao, Y., Zhang, C., Xiong, X., 2012, "Intergranular Corrosion Susceptibility of a Novel Super304H Stainless Steel," Engineering Failure Analysis, **24**(0) pp. 26-32.

[29] Gloyna, E. F., and Li, L., 1993, "Supercritical Water Oxidation: An Engineering Update," Waste Management, **13**(5–7) pp. 379-394.

[30] Gollapudi, S., 2012, "Grain Size Distribution Effects on the Corrosion Behaviour of Materials," Corrosion Science, **62**(0) pp. 90-94.

[31] Was, G. S., Teysseyre, S., and Jiao, Z., 2006, "Corrosion of Austenitic Alloys in Supercritical Water," Corrosion, **62**(11) pp. 989-1005.

[32] Gupta, G., Ampornrat, P., Ren, X., 2007, "Role of Grain Boundary Engineering in the SCC Behavior of Ferritic-Martensitic Alloy HT-9," Journal of Nuclear Materials, **361**(2-3) pp. 160-173.

[33] Guzonas, D. A., and Cook, W. G., 2012, "Cycle Chemistry and its Effect on Materials in a Supercritical Water-Cooled Reactor: A Synthesis of Current Understanding," Corrosion Science, **65**(0) pp. 48-66.

[34] Habicht, W., Boukis, N., Franz, G., 2004, "Investigation of Nickel-Based Alloys Exposed to Supercritical Water Environments," Microchimica Acta, **145**(1-4) pp. 57-62.

[35] Han En-Hou, Wang Jianqiu, Wu Xinqiang, 2010, "Corrosion Mechanisms of Stainless Steel and Nickel Base Alloys in High Temperature High Pressure Water," Acta Metallurgica Sinica, **46**(11) pp. 1379-1390.

[36] Hauthal, W. H., 2001, "Advances with Supercritical Fluids [Review]," Chemosphere, **43**(1) pp. 123-135.

[37] Hayward, T. M., Svishchev, I. M., and Makhija, R. C., 2003, "Stainless Steel Flow Reactor for Supercritical Water Oxidation: Corrosion Tests," The Journal of Supercritical Fluids, **27**(3) pp. 275-281.

[38] Hodes, M., Marrone, P. A., Hong, G. T., 2004, "Salt Precipitation and Scale Control in Supercritical Water oxidation—Part A: Fundamentals and Research," The Journal of Supercritical Fluids, **29**(3) pp. 265-288.

[39] Hu, H., Zhou, Z., Li, M., 2012, "Study of the Corrosion Behavior of a 18Cr-Oxide Dispersion Strengthened Steel in Supercritical Water," Corrosion Science, **65**(0) pp. 209-213.

[40] HUANG, S., DAEHLING, K., CARLESON, T., 1989, "Electrochemical Measurements of Corrosion of Iron-Alloys in Supercritical Water," ACS Symposium Series, **406**pp. 287-300.

[41] HUANG, S., DAEHLING, K., CARLESON, T., 1989, "Thermodynamic Analysis of Corrosion of Iron-Alloys in Supercritical Water," ACS Symposium Series, **406**pp. 276-286.

[42] Hwan, S. S., Lee, B. H., Kim, J. G., 2008, "SCC and Corrosion Evaluations of the F/M Steels for a Supercritical Water Reactor," Journal of Nuclear Materials, **372**(2-3) pp. 177-181.

[43] Hwang, S. S., Lee, B. H., Kim, J. G., 2008, "SCC and Corrosion Evaluations of the F/M Steels for a Supercritical Water Reactor," Journal of Nuclear Materials, **372**(2–3) pp. 177-181.

[44] Imre, A. R., Házi, G., Horváth, Á., 2011, "The Effect of Low-Concentration Inorganic Materials on the Behaviour of Supercritical Water," Nuclear Engineering and Design, **241**(1) pp. 296-300.

[45] Isselin, J., Kasada, R., and Kimura, A., 2010, "Corrosion Behaviour of 16%Cr-4%Al and 16%Cr ODS Ferritic Steels Under Different Metallurgical Conditions in a Supercritical Water Environment," Corrosion Science, **52**(10) pp. 3266-3270.

[46] Jang, J., Lee, Y., Han, C., 2005, "Effect of Cr Content on Supercritical Water Corrosion of High Cr Alloys," Pricm 5: The Fifth Pacific Rim International Conference on Advanced Materials and Processing, Pts 1-5, **475-479**pp. 1483-1486.

[47] Kanou, S., Takakuwa, O., Mannava, S. R., 2012, "Effect of the Impact Energy of various Peening Techniques on the Induced Plastic Deformation Region," Journal of Materials Processing Technology, **212**(10) pp. 1998-2006.

[48] Karakama, K., Rogak, S. N., and Alfantazi, A., 2012, "Characterization of the Deposition and Transport of Magnetite Particles in Supercritical Water," The Journal of Supercritical Fluids, **71**(0) pp. 11-18.

[49] Kaul, C., Vogel, H., and Exner, H., 1999, "Corrosion Behaviour of Inorganic Materials in Subcritical and Supercritical Aqueous Solutions," Materialwissenschaft Und Werkstofftechnik, **30**(6) pp. 326-331.

[50] Kessides, I. N., 2012, "The Future of the Nuclear Industry Reconsidered: Risks, Uncertainties, and Continued Promise," Energy Policy, **48**(0) pp. 185-208.

[51] Kim, H., Kurata, Y., and Sanada, N., 1999, "Corrosion of 316 stainless steel in supercritical water," pp. 65.

[52] Kim, H., Mitton, D. B., and Latanision, R. M., 2010, "Corrosion Behavior of Ni-Base Alloys in Aqueous HCl Solution of pH 2 at High Temperature and Pressure," Corrosion Science, **52**(3) pp. 801-809.

[53] Kirkham, M.B., 2005, "Principles of Soil and Plant Water Relations,"Academic Press, Burlington, pp. 27-40.

[54] Konys, J., Fodi, S., Hausselt, J., 1999, "Corrosion of High-Temperature Alloys in Chloride-Containing Supercritical Water Oxidation Systems," Corrosion, **55**(1) pp. 45-51.

[55] Kritzer, P., 2004, "Corrosion in High-Temperature and Supercritical Water and Aqueous Solutions: A Review," Journal of Supercritical Fluids, **29**(1-2) pp. 1-29.

[56] Kritzer, P., Boukis, N., and Dinjus, E., 2000, "Review of the Corrosion of Nickel-Based Alloys and Stainless Steels in Strongly Oxidizing Pressurized High-Temperature Solutions at Subcritical and Supercritical Temperatures," Corrosion, **56**(11) pp. 1093-1104.

[57] Kritzer, P., Boukis, N., and Dinjus, E., 1999, "Factors Controlling Corrosion in High-Temperature Aqueous Solutions: A Contribution to the Dissociation and Solubility Data Influencing Corrosion Processes," Journal of Supercritical Fluids, **15**(3) pp. 205-227.

[58] Kritzer, P., Boukis, N., and Dinjus, E., 1998, "The Corrosion of Alloy 625 (NiCr22Mo9Nb; 2.4856) in High-Temperature, High-Pressure Aqueous Solutions of Phosphoric Acid and Oxygen. Corrosion at Sub- and Supercritical Temperatures," Materials and Corrosion-Werkstoffe Und Korrosion, **49**(11) pp. 831-839.

[59] Kruse, A., and Dinjus, E., 2007, "Hot Compressed Water as Reaction Medium and Reactant: 2. Degradation Reactions," The Journal of Supercritical Fluids, **41**(3) pp. 361-379.

[60] Lee, H., Kim, D., Jung, J., 2009, "Influence of Peening on the Corrosion Properties of AISI 304 Stainless Steel," Corrosion Science, **51**(12) pp. 2826-2830.

[61] Leusbrock, I., Metz, S. J., Rexwinkel, G., 2010, "The Solubility of Magnesium Chloride and Calcium Chloride in Near-Critical and Supercritical Water," The Journal of Supercritical Fluids, **53**(1–3) pp. 17-24.

[62] Leusbrock, I., Metz, S. J., Rexwinkel, G., 2008, "Quantitative Approaches for the Description of Solubilities of Inorganic Compounds in Near-Critical and Supercritical Water," The Journal of Supercritical Fluids, **47**(2) pp. 117-127.

[63] Leybros, A., Roubaud, A., Guichardon, P., 2010, "Supercritical Water Oxidation of Ion Exchange Resins: Degradation Mechanisms," Process Safety and Environmental Protection, **88**(3) pp. 213-222.

[64] Bai, T., Chen, P., and Guan, K., "Evaluation of Stress Corrosion Cracking Susceptibility of Stainless Steel 304L with Surface Nanocrystallization by Small Punch Test," Materials Science and Engineering: A, (0).

[65] Lu, J. Z., Luo, K. Y., Yang, D. K., 2012, "Effects of Laser Peening on Stress Corrosion Cracking (SCC) of ANSI 304 Austenitic Stainless Steel," Corrosion Science, **60**(0) pp. 145-152.

[66] Lu, J. Z., Luo, K. Y., Zhang, Y. K., 2010, "Grain Refinement Mechanism of Multiple Laser Shock Processing Impacts on ANSI 304 Stainless Steel," Acta Materialia, **58**(16) pp. 5354-5362.

[67] Luo, X., Tang, R., Long, C., 2008, "Corrosion Behavior of Austenitic and Ferritic Steels in Supercritical Water," Nuclear Engineering and Technology, **40**(2) pp. 147-154.

[68] Macdonald, D., 2004, "Effect of Pressure on the Rate of Corrosion of Metals in High Subcritical and Supercritical Aqueous Systems," Journal of Supercritical Fluids, **30**(3) pp. 375-382.

[69] Marcus, Y., 2012, "Hansen Solubility Parameters for Supercritical Water," The Journal of Supercritical Fluids, **62**(0) pp. 60-64.

[70] Marr, R., and Gamse, T., 2000, "Use of Supercritical Fluids for Different Processes Including New developments—a Review," Chemical Engineering and Processing: Process Intensification, **39**(1) pp. 19-28.

[71] Marrone, P. A., and Hong, G. T., 2009, "Corrosion Control Methods in Supercritical Water Oxidation and Gasification Processes," Journal of Supercritical Fluids, **51**(2) pp. 83-103.

[72] Mordyuk, B. N., Karasevskaya, O. P., and Prokopenko, G. I., 2013, "Structurally Induced Enhancement in Corrosion Resistance of Zr–2.5%Nb Alloy in Saline Solution by Applying Ultrasonic Impact Peening," Materials Science and Engineering: A, **559**(0) pp. 453-461.

[73] Mordyuk, B. N., Karasevskaya, O. P., Prokopenko, G. I., 2012, "Ultrafine-Grained Textured Surface Layer on Zr–1%Nb Alloy Produced by Ultrasonic Impact Peening for Enhanced Corrosion Resistance," Surface and Coatings Technology, **210**(0) pp. 54-61.

[74] Mordyuk, B. N., Milman, Y. V., Iefimov, M. O., 2008, "Characterization of Ultrasonically Peened and Laser-Shock Peened Surface Layers of AISI 321 Stainless Steel," Surface and Coatings Technology, **202**(19) pp. 4875-4883.

[75] Mordyuk, B. N., Prokopenko, G. I., Vasylyev, M. A., 2007, "Effect of Structure Evolution Induced by Ultrasonic Peening on the Corrosion Behavior of AISI-321 Stainless Steel," Materials Science and Engineering: A, **458**(1–2) pp. 253-261.

[76] Becker, K. H., Cemič, L., and Langer, K. E. O. E., 1983, "Solubility of Corundum in Supercritical Water," Geochimica Et Cosmochimica Acta, **47**(9) pp. 1573-1578.

[77] Motta, A. T., Yilmazbayhan, A., da Silva, M. J. G., 2007, "Zirconium Alloys for Supercritical Water Reactor Applications: Challenges and Possibilities," Journal of Nuclear Materials, **371**(1–3) pp. 61-75.

[78] Murphy, M., 1996, "Blasting and Shot Peening," Metal Finishing, **94**(2) pp. 16-18.

[79] Muthukumar, N., Lee, J. H., and Kimura, A., 2011, "SCC Behavior of Austenitic and Martensitic Steels in Supercritical Pressurized Water," Journal of Nuclear Materials, **417**(1–3) pp. 1221-1224.

[80] Nie, S. H., Chen, Y., Ren, X., 2010, "Corrosion of Alumina-Forming Austenitic Steel Fe–20Ni–14Cr–3Al–0.6Nb–0.1Ti in Supercritical Water," Journal of Nuclear Materials, **399**(2–3) pp. 231-235.

[81] Novotny, R., Hähner, P., Siegl, J., 2011, "Stress Corrosion Cracking Susceptibility of Austenitic Stainless Steels in Supercritical Water Conditions," Journal of Nuclear Materials, **409**(2) pp. 117-123.

[82] Olmedo, A. M., Alvarez, M. G., Domínguez, G., 2012, "Corrosion Behavior of T91 and Type AISI 403 Stainless Steel in Supercritical Water," Procedia Materials Science, **1**(0) pp. 543-549.

[83] Peng, Q. J., Teysseyre, S., Andresen, P. L., 2007, "Stress Corrosion Crack Growth in Type 316 Stainless Steel in Supercritical Water," Corrosion, **63**(11) pp. 1033-1041.

[84] Potgieter, J. H., Olubambi, P. A., Cornish, L., 2008, "Influence of Nickel Additions on the Corrosion Behaviour of Low Nitrogen 22% Cr Series Duplex Stainless Steels," Corrosion Science, **50**(9) pp. 2572-2579.

[85] Ralston, K. D., Birbilis, N., and Davies, C. H. J., 2010, "Revealing the Relationship between Grain Size and Corrosion Rate of Metals," Scripta Materialia, **63**(12) pp. 1201-1204.

[86] Allen, T.R., Chen, Y., Ren, X., 2012, "Comprehensive Nuclear Materials,"Elsevier, Oxford, pp. 279-326.

[87] Ren, X., Sridharan, K., and Allen, T. R., 2007, "Corrosion Behavior of Alloys 625 and 718 in Supercritical Water," Corrosion, **63**(7) pp. 603-612.

[88] Ren, X., Sridharan, K., and Allen, T. R., 2006, "Corrosion of Ferritic-Martensitic Steel HT9 in Supercritical Water," Journal of Nuclear Materials, **358**(2-3) pp. 227-234.

[89] Saito, N., Tsuchiya, Y., Yamamoto, S., 2006, "Chemical Thermodynamics Consideration on Corrosion Products in Supercritical-Water-Cooled Reactor Coolant," Nuclear Technology, **155**(1) pp. 105-113.

[90] Schulenberg, T., Starflinger, J., Marsault, P., 2011, "European Supercritical Water Cooled Reactor," Nuclear Engineering and Design, **241**(9) pp. 3505-3513.

[91] Siwy, A. D., Clark, T. E., and Motta, A. T., 2009, "Transmission Electron Microscopy of Oxide Development on 9Cr ODS Steel in Supercritical Water," Journal of Nuclear Materials, **392**(2) pp. 280-285.

[92] Son, S., Lee, J., and Lee, C., 2008, "Corrosion Phenomena of Alloys by Subcritical and Supercritical Water Oxidation of 2-Chlorophenol," The Journal of Supercritical Fluids, **44**(3) pp. 370-378.

[93] Song, K. H., Kim, H. S., and Kim, W. Y., 2011, "Enhanced Grain Refinement and Mechanical Properties in a Severely Plastic Deformed Ni–30Cr Alloy," Materials Science and Engineering: A, **528**(27) pp. 7968-7973.

[94] Statnikov, E. S., Korolkov, O. V., and Vityazev, V. N., 2006, "Physics and Mechanism of Ultrasonic Impact," Ultrasonics, **44, Supplement**(0) pp. e533-e538.

[95] Sue, K., Kimura, K., Murata, K., 2004, "Effect of Cations and Anions on Properties of Zinc Oxide Particles Synthesized in Supercritical Water," The Journal of Supercritical Fluids, **30**(3) pp. 325-331.

[96] Sun, C., Hui, R., Qu, W., 2009, "Progress in Corrosion Resistant Materials for Supercritical Water Reactors," Corrosion Science, **51**(11) pp. 2508-2523.

[97] Sun, M., Wu, X., Han, E., 2009, "Microstructural Characteristics of Oxide Scales Grown on Stainless Steel Exposed to Supercritical Water," Scripta Materialia, **61**(10) pp. 996-999.

[98] Sun, M., Wu, X., Zhang, Z., 2009, "Oxidation of 316 Stainless Steel in Supercritical Water," Corrosion Science, **51**(5) pp. 1069-1072.

[99] Sun, M., Wu, X., Zhang, Z., 2008, "Analyses of Oxide Films Grown on Alloy 625 in Oxidizing Supercritical Water," The Journal of Supercritical Fluids, **47**(2) pp. 309-317.

[100] Tan, L., and Allen, T. R., 2009, "Localized Corrosion of Magnetite on ferritic–martensitic Steels Exposed to Supercritical Water," Corrosion Science, **51**(11) pp. 2503-2507.

[101] Tan, L., Allen, T. R., and Yang, Y., 2011, "Corrosion Behavior of Alloy 800H (Fe-21Cr-32Ni) in Supercritical Water," Corrosion Science, **53**(2) pp. 703-711.

[102] Tan, L., Anderson, M., Taylor, D., 2011, "Corrosion of Austenitic and Ferritic-Martensitic Steels Exposed to Supercritical Carbon Dioxide," Corrosion Science, **53**(10) pp. 3273-3280.

[103] Tan, L., Machut, M. T., Sridharan, K., 2007, "Corrosion Behavior of a ferritic/martensitic Steel HCM12A Exposed to Harsh Environments," Journal of Nuclear Materials, **371**(1-3) pp. 161-170.

[104] Tan, L., Ren, X., and Allen, T. R., 2010, "Corrosion Behavior of 9-12% Cr Ferritic-Martensitic Steels in Supercritical Water," Corrosion Science, **52**(4) pp. 1520-1528.

[105] Tan, L., Ren, X., Sridharan, K., 2008, "Corrosion Behavior of Ni-Base Alloys for Advanced High Temperature Water-Cooled Nuclear Plants," Corrosion Science, **50**(11) pp. 3056-3062.

[106] Allen, T. R., Sridharan, K., Tan, L., 2008, "Materials Challenges for Generation IV Nuclear Energy Systems," Nuclear Technology, **162**(3) pp. 342-357.

[107] Tan, L., Yang, Y., and Allen, T. R., 2006, "Oxidation Behavior of Iron-Based Alloy HCM12A Exposed in Supercritical Water," Corrosion Science, **48**(10) pp. 3123-3138.

[108] Tao, N. R., Sui, M. L., Lu, J., 1999, "Surface Nanocrystallization of Iron Induced by Ultrasonic Shot Peening," Nanostructured Materials, **11**(4) pp. 433-440.

[109] Teysseyre, S., Jiao, Z., West, E., 2007, "Effect of Irradiation on Stress Corrosion Cracking in Supercritical Water," Journal of Nuclear Materials, **371**(1-3) pp. 107-117.

[110] Teysseyre, S., and Was, G. S., 2006, "Stress Corrosion Cracking of Austenitic Alloys in Supercritical Water," Corrosion, **62**(12) pp. 1100-1116.

[111] Torgerson, D. F., Shalaby, B. A., and Pang, S., 2006, "CANDU Technology for Generation III+ and IV Reactors," Nuclear Engineering and Design, **236**(14–16) pp. 1565-1572.

[112] Wang, T., Yu, J., and Dong, B., 2006, "Surface Nanocrystallization Induced by Shot Peening and its Effect on Corrosion Resistance of 1Cr18Ni9Ti Stainless Steel," Surface and Coatings Technology, **200**(16–17) pp. 4777-4781.

[113] Ampornrat, P., Gupta, G., and Was, G. S., 2009, "Tensile and Stress Corrosion Cracking Behavior of Ferritic-Martensitic Steels in Supercritical Water," Journal of Nuclear Materials, **395**(1-3) pp. 30-36.

[114] Asselin, E., Alfantazi, A., and Rogak, S., 2010, "Corrosion of nickel–chromium Alloys, Stainless Steel and Niobium at Supercritical Water Oxidation Conditions," Corrosion Science, **52**(1) pp. 118-124.

[115] Watanabe, Y., and Daigo, Y., 2006, "Corrosion Rate and Oxide Scale Characteristics of Austenitic Alloys in Supercritical Water," High-Temperature Oxidation and Corrosion 2005, **522-523**pp. 213-219.

[116] West, E. A., and Was, G. S., 2009, "IGSCC of Grain Boundary Engineered 316L and 690 in Supercritical Water," Journal of Nuclear Materials, **392**(2) pp. 264-271.

[117] Withag, J. A. M., Sallevelt, J. L. H. P., Brilman, D. W. F., 2012, "Heat Transfer Characteristics of Supercritical Water in a Tube: Application for 2D and an Experimental Validation," The Journal of Supercritical Fluids, **70**(0) pp. 156-170.

[118] Xu, P., Zhao, L. Y., Sridharan, K., 2012, "Oxidation Behavior of Grain Boundary Engineered Alloy 690 in Supercritical Water Environment," Journal of Nuclear Materials, **422**(1–3) pp. 143-151.

[119] Yang, X., Zhou, J., and Ling, X., 2012, "Study on Plastic Damage of AISI 304 Stainless Steel Induced by Ultrasonic Impact Treatment," Materials & Design, **36**(0) pp. 477-481.

[120] YANG, Y., YAN, Q., and GE, C., 2012, "Hot Deformation Behavior of Modified CNS-II F/M Steel," Journal of Iron and Steel Research, International, **19**(1) pp. 60-65.

[121] YANG, Y., YAN, Q., YANG, Y., 2012, "Corrosion Behavior of Ferritic/Martensitic Steels CNS-I and Modified CNS-II in Supercritical Water," Journal of Iron and Steel Research, International, **19**(5) pp. 69-36.

[122] Yi, Y., Lee, B., Kim, S., 2006, "Corrosion and Corrosion Fatigue Behaviors of 9cr Steel in a Supercritical Water Condition," Materials Science and Engineering A-Structural Materials Properties Microstructure and Processing, **429**(1-2) pp. 161-168.

[123] Yin, K., Qiu, S., Tang, R., 2009, "Corrosion Behavior of ferritic/martensitic Steel P92 in Supercritical Water," Journal of Supercritical Fluids, **50**(3) pp. 235-239.

[124] Yongdong, H., Xinming, Z., and Zhiqiang, C., 2010, "Effect of Minor Cr, Mn, Zr, Ti and B on Grain Refinement of as-Cast Al-Zn-mg-Cu Alloys," Rare Metal Materials and Engineering, **39**(7) pp. 1135-1140.

[125] Yoon, J., Son, K., Kim, H., 2005, "Corrosion Behavior of 316L Stainless Steel in Supercritical Water Environment," Pricm 5: The Fifth Pacific Rim International Conference on Advanced Materials and Processing, Pts 1-5, **475-479**pp. 4207-4210.

[126] Zhang, L., Bao, Y., and Tang, R., 2012, "Selection and Corrosion Evaluation Tests of Candidate SCWR Fuel Cladding Materials," Nuclear Engineering and Design, **249**(0) pp. 180-187.

[127] Zhang, N., Xu, H., Li, B., 2012, "Influence of the Dissolved Oxygen Content on Corrosion of the ferritic–martensitic Steel P92 in Supercritical Water," Corrosion Science, **56**(0) pp. 123-128.

[128] Zhang, Q., Tang, R., Yin, K., 2009, "Corrosion Behavior of Hastelloy C-276 in Supercritical Water," Corrosion Science, **51**(9) pp. 2092-2097.

[129] ZHAO, Q., ZHANG, Z., CHENG, D., 2012, "High Temperature Corrosion of Water Wall Materials T23 and T24 in Simulated Furnace Atmospheres," Chinese Journal of Chemical Engineering, **20**(4) pp. 814-822.

[130] Zhong Xiangyu, Wu Xinqiang, and Han En-Hou, 2011, "Corrosion Behaviors of Nuclear-Grade Stainless Steel and Ferritic-Martensitic Steel in Supercritical Water," Acta Metallurgica Sinica, **47**(7) pp. 932-938.

[131] Zhong, X., Wu, X., and Han, E., 2012, "The Characteristic of Oxide Scales on T91 Tube After Long-Term Service in an Ultra-Supercritical Coal Power Plant," The Journal of Supercritical Fluids, **72**(0) pp. 68-77.

[132] Wang, R., 2012, “Effects of Oxide Additions on the Corrosion Behaviour of Cr2O3 Based Ceramics in High Temperature Supercritical Water Environment,” M.Sc. University of Alberta, Canada.

[133] Maranian, Peter, 2009, “Reducing Brittle and Fatigue Failures in Steel Structures,” New York: American Society of Civil Engineers.

[134] Baumeister, Avallone, Baumeister. Marks' Standard Handbook for Mechanical Engineers, 8th ed.. McGraw Hill. pp. 6-18,17.

[135] Worch, H. (1989), P. Kofstad, High Temperature Corrosion. Elsevier Applied Science, London/New York 1988, 546.

[136] McMullan, D., 1995, Scanning electron microscopy 1928–1965. Scanning, 17: 175–185.

[137] Joseph Goldstein, 2003. Scanning Electron Microscopy and X-Ray Microanalysis. Springer. ISBN 978-0-306-47292-3. Retrieved 26 May 2012.

[138] Andrej Šalak et al., 2011, “Effect of Manganese Addition and Sintering Conditions on Mechanical Properties of Low Carbon 3Cr Prealloyed Steels”, Materials Science Forum, 672, 55.

[139] Lucia Suarez et al., 2008, “Effect of Si on High-Temperature Oxidation of Steel during Hot Rolling”, Defect and Diffusion Forum, 273-276, 655.

[140] Stott, F. H., Wei, F. I. and Enahoro, 1989, “The influence of manganese on the High-temperature oxidation of iron-chromium alloys”, Materials and Corrosion, 40: 198–205.

Appendix 1: Parabolic Rate Constant Calculation.

Parabolic rate constant, k_p, expressed in $mg^2cm^{-2}h^{-2}$, is defined by

$$(\frac{\Delta M}{S})^2 = A + k_p t$$

in which ΔM is the weight change in mg, S is the area oxidation took place in cm^2 which is equal to the sample's surface area, A is a constant and t is the oxidation time.

$$\Delta M = M_1 - M_0$$

Where M_1 is the weight of sample after supercritical water exposure and M_0 is the weight before supercritical water exposure.

The following part use sample UP-FM-1 tested in 500 ℃, 25MPa supercritical water with 8 ppm dissolved oxygen as an example to show the calculation.

$$S = 2 * (L * W + L * H + W * H) = 2.122 cm^2$$

$$t = 100\ h, \quad \Delta M = M_1 - M_0 = 3.735 mg$$

$$t = 250\ h, \quad \Delta M = M_1 - M_0 = 7.056 mg$$

$$t = 500\ h, \quad \Delta M = M_1 - M_0 = 9.284 mg$$

$$t = 1000\ h, \quad \Delta M = M_1 - M_0 = 11.525 mg$$

Put ΔM, S and t in $(\frac{\Delta M}{S})^2 = A + k_p t$, using excel to calculate the value of A and k_p. A=5.878 and k_p=0.024.